Freestanding Non-Precious Metal Electrocatalysts for Oxygen Evolution and Reduction Reactions

Hao-Fan Wang[a,b§], Ruixuan Chen[a§], Jingyu Feng[a§], Mo Qiao[a§], Szymon Doszczeczko[a§], Prof. Qiang Zhang[a,b], Dr. Ana Belen Jorge [a,c*], Prof. Maria-Magdalena Titirici[a,c*]

[a] School of Engineering and Materials Science, Queen Mary University of London, London, E1 4NS, UK

[b] Beijing Key Laboratory of Green Chemical Reaction Engineering, Department of Chemical Engineering, Tsinghua University, Beijing, 100084, China

[c] Materials Research Institute, Queen Mary University of London, London, E1 4NS, UK

§ Authors contributed equally to this work.

Keywords: Electrochemistry; Energy Conversion; Freestanding; Oxygen Reduction Reaction; Oxygen Evolution Reaction;

Abstract

Carbon and transition metals have emerged as promising candidates for many energy storage and conversion devices. They facilitate charge transfer reactions whilst showing a good stability. These materials, fabricated as freestanding electrodes pose the potential of simplified electrode manufacturing procedures whilst demonstrating excellent electrocatalytic, mechanical and structural properties, resulting from inter-connected (via chemical or van der Waals force bonded) network structures. In such freestanding configuration, the lack of a binder leads to a better conductivity, ease in the manufacturing processing and allows a lower catalyst mass loading, all of which lead to obvious benefits.

This review summarizes different fabrication techniques of freestanding non-precious metal oxygen electrocatalysts along with their performance towards oxygen evolution reaction (OER) and / or oxygen reduction reaction (ORR). Here we discuss electrocatalysts produced using freestanding substrates and those obtained *via* self-assembly of different precursors. The advantages of using freestanding *versus* non-freestanding configurations are also pondered. Challenges and perspectives for freestanding electrocatalysts are presented at the end of the review as a guideline for future studies in the field. This work is expected to serve as inspiration for science colleagues to develop further studies into design, processing and testing strategies of freestanding low-cost oxygen electrocatalysts.

1. Introduction

The oxygen reduction and evolution reactions (oxygen reduction reaction (ORR) and oxygen evolution reaction (OER), respectively) involve complex electronic pathways which result in high overpotential and sluggish kinetics, and therefore, the bottleneck for further development of relevant energy technologies, including metal-air batteries, fuel cells and water electrolyzers. An efficient, stable and low cost electrocatalyst would translate into economically feasible implementation of those technologies, which would form a foundation for a sustainable energy economy.

Over the past few years, various materials have been employed in oxygen electrocatalysis.[1] Among them, traditional precious metals catalysts have consistently

achieved high performance.[2] However their applications are limited by their high cost and scarcity.[3] For this reason, and due to the recent development of electric vehicles, precious metal-free materials have attracted great interest as alternative low-cost sustainable electrocatalysts, exhibiting competitive electrocatalytic activity.[4] Among them, transition metal compounds and carbon-based nanomaterials including: metal oxides (spinels, perovskites), hydroxides, sulphides, heteroatom-doped carbon, defective carbon and carbon nitrides have been demonstrated to be promising substitutes.[5]

Most of the catalysts tested in powder form are drop-casted onto a rotating disk electrode (RDE) or rotating ring-disk electrode (RRDE) to evaluate their electrochemical performance. This configuration allows us to achieve system conditions where the steady-state current is not controlled by the diffusion of species in the electrolyte, but by the static flow generated by the electrode rotation, which in turn provides information on electron transfer kinetics and electrochemical reaction mechanisms. The catalyst coating on the electrode requires the assistance of a binder, thus featuring the disadvantages of high resistance and low stability. This results in the potential dissolution of the binder into the electrolyte during the cycling process which in turn would trigger the detachment of the catalyst from the rotating disc electrode.[6] Freestanding materials can be processed in a three-dimensional (3D) morphology without the assistance of additives or extra substrates, and exhibit compact structure, excellent mechanical properties, high mass loading as well as efficient internal mass

and charge transfer, which would potentially lead to much higher current density and stability, when compared to powdered oxygen electrocatalysts.[7] However, using RDE or RRDE is more challenging when working with freestanding electrocatalysts, as they need to be cut into pieces of size matching that of the glassy carbon RDE / RRDE. Although, this process may seem easy, attaining precise, reliable and reproducible RDE / RRDE data using freestanding electrocatalysts is not straightforward and requires some special research skills.

Moreover, in some practical applications such as fuel cells and metal-air batteries, an air electrode with hierarchical porous structure is highly recommended for gas diffusion requirements.[8] In the case of conventional powder catalysts, 3D substrates are commonly applied to fabricate air electrodes, which involve further steps and therefore increase the complexity of their manufacture. Moreover, the interface catalyst coating - substrate further leads to the further problems in resistance, stability and low mass loading.[9] Additionally, fabrication of air electrodes of metal-air batteries is requires a bifunctional electrocatalyst active towards both OER and ORR.

Up to date, much efforts have focused on producing freestanding electrodes across different fields, leading to excellent reviews on materials synthesis, manufacturing strategies, and the applications in energy, environment and healthcare.[6, 10] The present review will only focus on freestanding materials for oxygen electrocatalysis (Scheme 1). Freestanding oxygen electrocatalysts have been divided into two main groups,

according to whether they are deposited onto existing commercial skeletons that also contribute to the electrocatalytic activity in the electrocatalytic process, or self-supported oxygen electrocatalysts. The active materials employed, their structural features, physicochemical characterization, electrochemical testing methods and electrocatalytic activity are also discussed. We are confident this review will inspire more research devoted to creating highly efficient freestanding oxygen electrocatalysts, and their incorporation into sustainable energy technologies.

2. Fabrication of freestanding materials for oxygen electrocatalysis

Efficient oxygen electrocatalysts possess specific structural characteristics which, when fabricated into a freestanding form, must be preserved for the catalyst to perform comparatively. Primarily, an electrocatalyst structure must facilitate oxygen, electrolyte, and electrons accessibility to the active sites. Consequently, oxygen electrocatalysts are usually designed to have a hierarchical porous structure resulting in high surface area and abundant channels for gas and electrolyte transfer accompanied by high electrical conductivity.[11] Fabrication techniques leading to the formation of such appropriate structures can be classified into two categories: (1) substrate-supported fabrication, which involves the deposition of the catalytic material on a pre-existing substrate (usually the case for transitional metal materials and part of carbon-based electrocatalysts); and (2) self-fabrication of suitable skeleton which itself

represents the catalytic material (commonly for self-assembly monolithic carbon-based materials).

2.1. Substrate-supported fabrication

This strategy involves the use of an existing 3D substrate as the skeleton. The substrates typically include metal foams such as Ni foam and Co foam, as well as other metals in form of foam or foil.[7, 9, 12] Carbon substrates such as carbon fiber-based flexible paper and cloth are also widely applied.[13] The active materials are then deposited on the substrate to form a strong chemical bond connection, leading to the formation of a composite structure.[14] The active material can also be loaded onto the substrate framework by *in situ* growth of nanoparticles on the surface of the skeleton.[15] In other cases, the active sites are directly derived from the substrates through oxidation, etching or doping.[13g, 13i, 13j] Typically, carbon fiber-based flexible paper has been used in energy storage devices such as Zn-air batteries serving as the catalysts carrier and support for hydrophobic layer utilized to facilitate the gas diffusion.[5d, 16] Meanwhile, metal foams are usually applied to energy conversion devices such as water electrolysers due to their intrinsic electrocatalytic activity.[17]

2.1.1. Electrochemical deposition techniques

Electrodeposition techniques involve the deposition of metal precursors or carbon nanomaterials previously present in an electrolyte bath by applying a voltage to the substrate material (which also acts as electrode). The technique has been widely used

to deposit both carbon and metal materials producing freestanding electrocatalysts on a variety of substrates, including stainless steel mesh and Ni foam.[6] One example of freestanding OER electrocatalyst prepared using this technique is the deposition of a highly active amorphous mesoporous nickel–iron composite nanosheets on a Ni foam, by using nickel nitrile and iron nitrile precursors in hydrochloric acid as electrolyte.[7] By varying the voltage applied and electrolyte composition, electrodeposition techniques enable precise control of the nucleation and growth processes, as well as the purity, structure and morphologies of the deposits obtained.[18] Furthermore, due to facile one-step approach, this synthesis is promising in large-scale fabrication.

2.1.2 Chemical vapour deposition

Chemical vapour deposition with its many variations, including aerosol assisted vapour deposition or plasma enhanced vapour deposition, typically consists of exposure of a substrate to volatile precursors which react and/or decompose on the substrate surface to produce the desired product.[19] Fabrication of freestanding materials for electrocatalysis with a foam-like structure has been demonstrated using template-directed chemical vapour deposition of graphene onto nickel foam, followed by coating with PMMA and etching with HCl and acetone.[20] Other approaches involved pre-treatment of a carbon paper substrate with oxygen plasma and coating with Al_2O_3, which allowed for vertical growth of carbon nanotubes, followed by further deposition of nickel cobalt sulphide and poly-pyrrole using a plasma-enhanced chemical vapour

deposition reactor.[21] Direct growth of nitrogen-doped carbon nanotubes on metal foams has been demonstrated to produce freestanding air cathode for Zn-air batteries which demonstrated remarkable performance.[22] Vapour deposition techniques have the potential of creating porous composite structures with superior electrical conductivity, excellent mechanical properties and offer high degree of control over the final microstructure.

2.1.3. Hydrothermal deposition

Hydrothermal deposition comprises sealing a substrate, typically metal foams, along with precursors of a second component to be deposited, into a Teflon inlet, and applying temperature over prolonged period of time leading to the growth or deposition of nanostructures onto the substrate material.[12c, 23] Other than commonly used carbonaceous materials, metal ions could also be employed for hydrothermal deposition, diffusing into the substrate during the thermal treatment to form nanoparticles.[24] A substrate may further be imparted with balanced hydrophobic and hydrophilic properties which had been shown to enhance oxygen diffusion and surface wetting and improving the electrocatalytic performance, oxygen diffusion and increasing conductivity.[11, 25]

Hydrothermal methods are frequently chosen for deposition or growth of electroactive materials as well as for modifying the chemical properties of the substrate. They represent an environmentally friendly and cost-effective approach that promote the

formation of a well-connected active material/substrate interface great with controllable nanostructure and surface chemistry.[26]

2.2. Self-fabricated electrocatalysts

Efficient electrocatalysts can also be prepared through the synthesis of self-supported structures with the appropriate porosity and active sites, necessary to catalyse the oxygen electrocatalytic reactions. Such synthetic procedures typically involve agglomeration, cross-linking or polymerization of building blocks like metal organic frameworks (MOFs), small organic molecules, transition metal compounds and carbon nanomaterials (CNTs, graphene and others.) to form porous 3D structures so-called foams, sponges and aerogels. [15, 27] Carbon materials are predominantly prepared using self-fabricated technique, due to their ease of manufacture and modulation relatively to metals.

2.2.1. Hydrothermal Methods

Similarly to substrate-supported electrocatalysts, hydrothermal treatment can also be applied to develop either monolithic carbon-based materials which can be shaped into different forms of standing electrodes, or graphene/CNT based composites, which can be subsequently mechanically pressed into freestanding pellets.[28] Both of the above strategies are widely applied in carbon-based materials hydrothermal synthesis.[29] The introduction of additional precursors during the hydrothermal treatment can lead to heteroatom doping or else to the introduction of transitional metals-based nanoparticles

within the carbon matrix to provide additional efficient active sites.[24a] Post-treatment such as annealing processes can further promote the assembly/stabilization of the active sites.

2.2.2. Film Casting

Film casting has also been applied to create flexible films from solutions or suspensions *via* evaporation or vacuum filtration.[30] Vacuum filtration is most commonly applied due to its scalability, reproducibility, efficiency and high degree of control over the film thickness.[31] The procedure relies on utilizing a semi-permeable membrane (e.g. filter paper) designed to stop the constituents of the film while permitting passage of the solvent under applications of vacuum used to generate the pressure necessary for the solvent movement. However, the transfer of the ultrathin film from the undesired substrate (e.g. filter paper) is usually challenging.[32] Film casting methods are widely used for carbon materials, carbon nanotubes, carbon fibers, and graphene nanosheets to enhance the mechanical strength and conductivity of the films.[33] This method requires relative simple operation and is applied to cast ultrathin films in thickness of micrometer scale.[34]

2.2.3. Electrospinning

Electrospinning is a fiber production method that employs an electric field to draw charged threads from a polymer solution or polymer melt up to fiber diameters in the nanometer scale.[35] The carbonization of the polymer fibers yield a conductive

nanofiber network with controllable fiber porosity. Inorganic active sites or heteroatom dopants can be introduced also during electrospinning by selecting suitable precursors.[36] This method affords the advantages of allowing high degree of control over the final electrocatalyst morphology as well as relatively low processing cost and scalability. A relatively simple preparation of a freestanding electrocatalyst with activity towards ORR *via* electrospinning has been demonstrated by Liu *et al*., who electrospun polyacrylonitrile subsequently carbonized under nitrogen and etched with ammonia to increase the nitrogen dopant content in the fibers. Unfortunately, some complications in the synthesis led to low reproducibility of the results.[12c]

2.2.4. Hard Templating

Templating is widely used for the synthesis of nanostructured materials. A variety of templates have been extensively applied to synthesize morphology-controllable nanostructures, such as hollow and mesoporous, with preserved 3D structure after the removal of the templates.[37] Metal foams such as Ni foam have been reported to serve as hard templates for the construction of freestanding electrodes, showing a well-structured macro-porous structure.[17] Templating methods provide a precise control over the resulting catalysts and lead to the desired hierarchical porous structures thus contributing to the oxygen diffusion and the creation of highly active sites.[20, 38] The removal of the hard template in some cases still remains a critical problem, which requires aggressive etching.

2.2.5. 3D Printing

Additive manufacturing techniques offer the prospect of allowing fine tuning of the structure and composition of the final electrode, allowing the fabrication of complex geometries at a low processing cost with minimal material wastage.[39] A wide range of nanostructured compounds can be dispersed in common solvents together with a binding polymer to form inks that can be extruded through the printer nozzle mounted on a three-axis motion stage, capable of accurately layering a porous electrode structure, preliminarily designed utilizing CAD software. In 2018, the first 3D printed freestanding cathode for Li-O_2 was reported.[40] A nanoporous graphene oxide ink in water was extruded into a highly porous mesh. In this case, however, the authors employed ruthenium salt, a noble metal, to enhance OER/ORR activity. Other efforts such as the creation of freestanding stretchable electrode *via* 3D printing of carbon nanotubes with polydimethylsiloxane in ethyl acetate solvent, demonstrate the potential of this technique in self-supported electrocatalyst manufacturing.[40-41]

2.3. Other techniques

Other technique for self-supported freestanding oxygen electrocatalysts worth mentioning is the flow-directed assembly, which has been shown to produce freestanding graphene oxide films with controllable thickness. One can easily imagine extending this technique to create modified graphene oxide with electrocatalytic properties whilst inducing further porosity using salt activation techniques and heat

treatment.[42] Electropolymerization techniques, which relay on the polymerization reaction occurring on a conductive substrate submerged in the monomer solution induced by application of electrical potential, has recently been used to electrodeposit Ni nanoparticles on Ni foam followed by electropolymerization of aniline, producing a freestanding electrocatalyst active towards hydrogen evolution reaction.[43]

Frequently, multiple fabrication strategies are used in conjunction with one another, for example, carbon substrate can be decorated with nanostructures through hydrothermal treatment followed by electrodeposition and chemical treatment such as sulfuration to incorporate nanosheets/nanoparticles.[13h, 44]

3. Freestanding materials for oxygen electrocatalysis

3.1. OER electrocatalysis

Non-noble metal freestanding OER electrocatalysts have received a great deal of attention as a consequence of the increasing cost and global scarcity of current state-of-the-art precious metals. In the case of water oxidation or oxygen evolution, carbon-based materials and transitional metal compounds supported on metal foam (e.g. Ni, Co) have shown great promise as freestanding electrocatalysts for OER.[45] Carbon-based materials are usually highly conductive and provide a high degree of control over the micro and macro porosity of the final structure, making them an attractive choice for OER electrocatalysis.[1c, 46] Unfortunately, carbonaceous materials are prone to oxidation during the OER.[47] At 1.23 V, which is the theoretical thermodynamic

potential for OER to occur, the thermodynamically favourable oxidation of carbon to carbon dioxide and carbon monoxide takes place instead of oxygen evolution in acidic media.[47] Carbon stability has been improved by creating structures with a high degree of graphitization.[48] In the case of transition metal compounds deposited onto metal foams, the limited conductivity, and reactivity of catalytic surface as well as stability often pose problems.[49] Some of these limitations have been effectively overcome through strategies such as the *in situ* growth of the electroactive material on the substrate or by pyrolysis of the electrode.[50]

3.1.1. Transition metal compounds on pre-formed skeletons

Transition metal (Fe, Co, Ni, etc.) compounds have been widely investigated as OER electrocatalysts.[5b, 51] Most of transition metal catalysts are synthesized in the form of powder, exhibiting various nanostructures with the purpose of enlarging the surface area. To fabricate freestanding electrocatalysts, these nanoparticles are often deposited on 3D skeletons such as metal foams, metal foils, and carbon-based materials (carbon fiber paper, carbon cloth, etc.), usually showing high electrical conductivity and high mechanical strength.[49c, 52] Some of the metal skeletons are also electroactive for OER.[53] Herein, transition metal-based oxygen electrocatalysts deposited onto 3D skeletons for OER electrocatalysis are discussed.

Ni foam

Commercial Ni foam is the most commonly used skeleton for freestanding OER catalysts.[6] Various kinds of transition metal compounds supported on Ni foam have

been reported as OER electrocatalysts, including layered double hydroxides (LDHs), perovskites, sulphides, and phosphides.[9, 12k, 54] Sun et al. reported a NiFe LDH film deposited on Ni foam as OER electrocatalyst.[55] **Figure 1**a presents the optical images of Ni foam before and after the deposition of LDHs. Ni foam shows a 3D monolithic structure with a brown film of NiFe LDH nanosheets coated on the surface via hydrothermal deposition. In the scanning electron microscopy (SEM) images of Figure 1b and 1c, LDH nanosheets with diameter of around 100 nm can be seen grown vertically on the Ni foam substrate. The OER activity of the NiFe LDH-based freestanding electrocatalyst is presented in Figure 1d-1f, including the linear sweep voltammetry (LSV) plots, Tafel plots and stability test. The Ni foam supported NiFe LDH achieved an OER current density of 30 mA cm^{-2} at a small overpotential of 280 mV, and Tafel slope of only ~50 mV dec^{-2}, surpassing the performance of commercial IrO_2 catalyst. This freestanding electrocatalyst also showed excellent stability as suggested by negligible degradation of the OER current density after 10 h potentiostatic testing.

Besides LDH, other kinds of transition metal compounds deposited on Ni foam with high OER activity were also reported. Recently synthesized CoP mesoporous nanorod arrays on conductive Ni foam led to a performance comparable to that of IrO_2 (1.52 V *vs*. reversible hydrogen electrode (RHE) at 10 mA cm^{-2}) and even higher stability than IrO_2 (91.5% current density retention, after 32 h, and 1.54 V *vs* RHE at 10 mA cm^{-2} for 32 h, whereas state-of-the-art IrO_2 only retained 53.4% current density).[12b]

Unfortunately, this was only true at low current densities. Also, promising is the work by Wang *et al*., who created a self-supported 3D porous nickel phosphide (Ni-P) foam, with a Ni_2P skeleton with vertically aligned Ni_5P_4–NiP_2 nanosheets that exhibited a current density of 191 mA cm^{-2} at an overpotential of 350 mV in 1.0 M KOH as well as long-term stability (10 mA cm^{-2} at 1.45 V *vs.* RHE for 26 h).[12h]The good performance of this compound was attributed to the formation of $NiO/Ni(OH)_x$, producing a Ni-P/$NiO(Ni(OH)_x)$ heterojunction.[12h] Another highly efficient OER electrocatalyst, based on ferrous metaphosphate on self-supported conductive nickel foam $Fe(PO_3)_2$ Ni_2P/Ni foam, exhibited excellent electrochemical performance, with an overpotential of only 218 mV in 0.1 M KOH, at 10 mA cm^{-2}.[56] When compared to state-of-the-art IrO_2, $Fe(PO_3)_2$ would only need 273 mV overpotential to yield 500 mA cm^{-2} current density, compared to the 380 mV overpotential needed for IrO_2. XPS analysis indicated that the plateau was attributed to the amorphization of $Fe(PO_3)_2$ and formation of FeOOH. This corroborated another study which revealed that FeOOH deposited onto Ni foam was a remarkable OER electrocatalyst.[57] It has also been reported that trace amounts of Fe in NiO_x/NiOOH would lead to a significant improvement in electrocatalytic activity.[58] Amongst other examples of electrocatalyst utilizing Ni foam substrate is P-doped Co_3O_4 which impressively achieved a current density of 10 mA cm^2 at an overpotential of 280 mV and Tafel slope of 51.6 mV dec^{-1}.[59] The doping has been performed using a novel approach consisting of irradiation in the presence of phosphorous source of the electrodeposited Co_3O_4 with Ar plasma,

designed to increase the number of oxygen vacancies subsequently filled by phosphorous atoms.[59]

In these works, the Ni foam skeletons provided metal frameworks for electron transport, macropores for gas diffusion, and large catalyst loading amount. The Ni foam itself is also active for OER electrocatalysis, as its surface is oxidized to oxides at high potential.

Other metal foams

Besides Ni, Co, and Fe foams can also serve as the skeleton of freestanding OER electrocatalysts. Co and Fe foams have the structure similar to that of Ni foams, and also possess the advantages such as high conductivity and intrinsic OER activity. In 2017, a cobalt foam supported Co_9S_8 catalyst was reported by Liu *et al*.[12f] This catalyst exhibited an overpotential for 10 mA cm^{-2} OER current density (η_{10}) of 350 mV, a high OER current density up to more than 300 mA cm^{-2}, and a small Tafel slope of 55 mV dec^{-1}. The same group also synthesized CoP nanowires grown on Co foam as OER electrocatalyst, reporting a low η_{10} (248 mV), and high current density (more than 300 mA cm^{-2})..[12e] Fe foam was used as catalyst substrate by Chen *et al*.[12a] in a study where $NiFeO_x$ was coated on Fe foam and tested as OER electrocatalyst, in 1.0 M KOH. A current density of 5 mA cm^{-2} and 1000 mA cm^{-2} were achieved at overpotentials of 220 and 300 mV, respectively. These works indicate that Co and Fe foams are good alternatives to Ni foams.

Stainless steel mesh

Recently, Zhang *et al.* reported $Ni(Fe)O_xH_y$ on stainless steel mesh as OER electrocatalyst.[60] The OER current density reached 20 mA cm^{-2} at the overpotential of 0.23 V *vs* RHE, and surpassed 400 mA cm^{-2} at an overpotential below 1.6 V *vs* RHE. Summarizing, the porous 3D metal skeletons, including metal foam and metal mesh, constitute an excellent group of materials to serve as skeletons of freestanding OER electrocatalysts.

Metal foil

Compared with metal foams, metal foils are non-porous, and have lower specific surface area. Therefore, metal foils are not often utilized as OER electrocatalyst substrates. Xu's group synthesized cobalt phosphides on cobalt foil for OER electrocatalysis.[61] The Co-foil supported catalyst showed a low η_{10} of 319 mV in 1.0 M KOH solution. They also reported a Ni-Fe sulfide catalyst grown on NiFe alloy foil, and the catalyst also exhibited excellent OER performance with an η_{10} of 282 mV in 1.0 M KOH.[62] However, the current densities at high overpotential of the metal foil supported catalysts were inferior to that of the metal foam/mesh supported catalysts. At 1.7 V *vs* RHE, the OER current densities of both catalysts were less than 100 mA cm^{-2}, which could be attributed to the relatively low catalyst loading amount on the metal foil substrates compared to porous alternatives.

Carbon substrates

Compared with metal skeletons, carbon-based skeletons show lower stability at high overpotential; however, their unique characteristics such as high electric conductivity

and tuneable hierarchical pore structure, which benefit for charge and mass transfer have made them widely applied as substrates for OER electrocatalysts. In 2015, Liu's group designed a flexible oxygen evolution electrode by depositing $NiCo_2O_4$ core-shell nanowires on carbon cloth.[13l] The η_{10} of the flexible OER catalyst was 320 mV, and the Tafel slope was 47.4 mV dec^{-1}. At the overpotential of about 450 mV, the current density achieved 300 mA cm^{-2}. Up to now, many kinds of transition metal compounds deposited on carbon-based skeletons have been reported to exhibit excellent OER performance. Some examples include nickel borate on carbon cloth, Co-doped ZnO on carbon fabric, Co_4N on carbon cloth, and nickel phosphide on carbon fiber paper.[13f, 13k, 63]

Transition metal-based OER electrocatalysts have high intrinsic activity. When fabricated as freestanding materials, the structural features of the skeletons can be modified to further enhance the OER performance, towards low overpotential and high current density. The OER performance of the freestanding OER electrocatalysts discussed above are listed in Table 1.

3.1.2. Carbon-based materials

Carbon materials such as carbon nanotubes (CNTs), graphene, or carbon nanoribbons are an attractive class of materials for electrocatalysis due to their large specific surface area, high electrical conductivity and easily tuneable structure.[64] These materials are typically modified through heteroatom doping or defect engineering prior to their use as freestanding electrocatalysts due their intrinsically low electroactivity. Heteroatom

doping involves carbon substitution by more electronegative atoms such as nitrogen or oxygen causing redistribution of electron density which renders the adjacent carbon atoms more positively charged leading to its stronger affinity towards the reaction intermediates. Similarly, topological and edge defects in graphitic carbon materials introduced during heat treatment or by chemical means result in breakage of charge neutrality.[65] Both induce a more optimal adsorption of the OH^- ions and hence the energy barrier for recombination of intermediates such as O^{2-} and O_2^{2-} to O_2 decreases, as described by Sabatier principle.[13i, 28a, 66] The highly electroactive carbon material can subsequently be processed into a self-supported hydrogel or foam by utilizing filtration, chemical reduction or hydrothermal treatment.

Self-fabricated carbon-based electrocatalysts

The high attainable electrocatalytic performance of such self-supported electrocatalyst has been demonstrated by Qiao *et al.*, who fabricated nitrogen and oxygen co-doped graphene-CNT composite hydrogel films by utilizing filtration to induce layer-by-layer assembly of chemically converted graphene and carbon nanotubes, followed by further nitrogen doping under ammonia gas at elevated temperature and pressure.[28a] The film displayed a low onset potential of 315 mV in 0.1 M KOH electrolyte reaching the current density of 5 mA cm^{-2} and 14.8 mA cm^{-2} at overpotentials of 368 mV and 564 mV respectively, exceeding the performance of traditionally used IrO_2 (**Figure 2**a). Moreover the electrocatalyst exhibited high durability in alkaline electrolytes with less than 20% anodic current loss during 800 continuous potential cycles further verified by

chronoamperometric analysis showing insignificant performance attenuation after operation for 5000 s (Figure 2b).[28a] Other efforts by the Qiao's group included the synthesis of a hybrid N-doped carbon/$NiCO_2O_4$ electrocatalyst also achieved using chemical modification and filtration of graphene to obtain porous graphene film hybridized by heterogeneous reaction with metal salts at elevated temperature.[67] The catalyst reached current densities of 5 mA cm^{-2} and 21.1 mA cm^{-2} at overpotentials of 373 and 564 mV exceeding the performance of pure $NiCO_2O_4$ electrocatalyst.

Substrate-supported fabrication of carbon-based electrocatalysts

In other work by Qiao *et al.*, cellulose based paper was used as a framework onto which graphene oxide and carbon nitride were deposited by dip coating and subsequently reduced and nitrogen-doped using hydrazine. This electrocatalyst film delivered the current density of 10 mA cm^{-2} at 414.5 mV overpotential.[68] Unfortunately, this multistep method proved to be too complicated and required relatively expensive graphene oxide precursor along with large amounts of acids, oxidants, and toxic reducing agents, limiting their commercial applicability. Yu *et al.* attempted to address this by fabricating a nitrogen and sulphur co-doped graphite foam (NSGF) from commercially available graphite foil (GFL) as freestanding OER electrode.[69] This fabrication strategy used a cheaper hydrothermal treatment instead, thermal treating graphite foil with thiourea as dopant followed by a simple washing step. The electrode achieved a current density of 10 mA cm^{-2} at an overpotential of only 380 mV in 0.1 M KOH. The stability tests showed less promising results with retention of only 77% of

the initial current density.[69] Qiao's group recently transformed commercially available carbon fiber paper into electroactive nitrogen doped graphene foam in a two-step process involving electrochemical expansion followed by chemical doping.[70] The electrocatalyst achieved 10 mA cm^{-2} at the overpotential of 380 mV. The electrocatalyst showed encouraging stability with current density decay of only 4.8% after a 16 h of constant operation at potential of 1.61 V and minimal activity diminishment during 5000 accelerated cyclic voltammogram cycles as Zn-air battery electrode.

In summary, noble-metal free carbon catalysts show a great promise as alternative OER electrocatalyst for application in water splitting, exceeding noble metal efficiencies, while issues of stability are less prominent. Difficulty in the control of porosity and defect distribution or lack of site selectivity during doping remain a challenge.[71] Recent fabrication methods such as 3D printing, vapour deposition methods or novel combinations of more traditional manufacturing techniques will provide the feasibility of mediating them.

3.2. ORR electrocatalysis

The oxygen reduction reaction (ORR) is a pivotal reaction resulting in breakage of the oxygen-oxygen bond of molecular oxygen, enabling release of energy though biological respiration, with its kinetics predominantly determining the efficiency and stability of fuel cell cathodes and discharge characteristics of metal-air batteries. Currently commercialized Pt group electrocatalysts suffers the problems of scarcity and easily degradation, so that noble-metal free materials with outstanding catalytic activity

and sustainability has demonstrated great potential as alternative electrocatalysts.[13d, 72] Great progress has been achieved in precious metal free electrocatalysts in recent years, some of which demonstrated comparable ORR catalytic activity and long term stability compared with commercial Pt.[13d, 72a, 73] Freestanding electrocatalysts demonstrated unique advantages such as interconnected hierarchical pore structure which facilitated mass and charge transfer.[6] However, studies on freestanding electrode ORR catalysts are still rare, the big limitation being the lack of a three-dimensional pore structure that can effectively diffuse oxygen, as well as suitable testing methods.[13h] Compared to the OER, the ORR is highly dependent on the access of molecular oxygen which is a reactant for ORR reaction, to the active site.[74] This access is usually provided by a gas (oxygen) flow generated by the electrode rotation during characterization, so that the steady-state current is not controlled by the diffusion of species in the electrolyte. Recently some researchers have reported an approach to test ORR while maintaining the freestanding feature.[13h, 17, 75] This involved cutting the freestanding catalyst into a small piece of precisely the size of the glassy carbon disc and sticking it onto the RDE/RRDE with addition of small amount binder.[17, 75]

3.2.1. Self-fabricated electrocatalysts

Liu *et al.* reported free-standing nitrogen-doped carbon electrospun nanofibers (N-CNF) based on polyacrylonitrile (PAN (**Figure 3a**, b)).[75] They were tested by placing a piece of freestanding electrocatalyst onto the RDE. This approach seemed to improve the gas transport during ORR because the RDE created a static flow rate to promote the

gas diffusion. The ORR onset potential and half-wave potential for the N-CNF freestanding electrocatalyst were –0.034 and –0.182 V, respectively, where the onset potential was about 45 mV more negative than commercial Pt/C catalyst (Figure 3c). Moreover, N-CNF exhibited 6.6% drop of current density after 10,000 s under continuous operation while Pt/C showed 16.3% drop of current density (Figure 3d). The comparable onset potential of N-CNF was attributed to the N-induced charge redistribution and the hydrophilicity of N-CNF, while the superior stability of N-CNF has been attributed to its free-standing structure.

3.2.2. Substrate-assisted electrocatalysts

Similarly, Cai *et al.* reported N-doped vertically aligned carbon nanotubes supported on graphene foam (N-VA-CNTs/GF).[17] The electrocatalytic activity was tested by adhering a piece of N-VA-CNTs/GF film on RDE.[76] The fabrication route of these N-VA-CNTs/GF is illustrated in **Figure 4**a. Chemical vapour deposition (CVD) was first applied to form graphene foam (GF) on Ni mesh followed by impregnation with catalysts and growth of vertically aligned carbon nanotubes (VA-CNTs). The Ni mesh was removed by an etching process followed by coating with PANI to produce N-VA-CNTs/GF. The electrochemical testing was then conducted by cutting N-VA-CNTs/GF films into 1mm diameter pieces and sticking them on the surface of glassy carbon with a 1 µL 0.5 wt% of Nafion solution. As illustrated in Figure 4b, VA-CNTs/GF sample annealed at 800°C exhibited comparable limiting current density to commercial 40% Pt/C catalysts. The durability studies showed that VA-CNTs/GF suffered 11% drop of

current density after 10,000 s of operation while Pt/C showed 50% drop of current density after 20,000 s of operation (**Figure 4c**). It is worth-noting that, although the GF films were thick and the RRDE testing might not provide the sufficient data to evaluate their activity, this could be a convenient way of comparing different catalysts under the same testing conditions.

A popular method of increasing the number of triple phase points in fuel cell cathodes is application of a thin and highly hydrophobic micro-porous layer on the substrate material leading to reduction of the liquid saturation in the catalyst layer.[77] The method was firstly used on noble metal electrocatalysts by application of poly(tetrafluoroethylene) (PTFE) hydrophobic agents onto Teflon treated carbon fiber papers loaded Pt/C catalyst, boosting oxygen diffusion though the cathode. Similarly Lu *et al*. illustrated a 'superaerophilic' free-standing structure by growing porous cobalt-incorporated nitrogen-doped carbon nanotube (CoNCNTs) arrays on carbon fibre paper (CFP) with PTFE post treatment.[13h] Compared to commercial Pt/C loaded carbon fiber paper (**Figure 5**a-d,), CoNCNTs possessed abundant three-phase contact point (TPCP) which was obtained through this 'superaerophilic' construction, and greatly increased the utilization of electrocatalysts and catalytic efficiency. The electrochemical performance of this free-standing electrode was measured in a three-electrode glass cell with O_2 bubbled through the electrolyte. CoNCNTs showed a lower onset potential than Pt/C catalyst on PTFE coated Teflon treated carbon fiber paper, due to the intrinsic catalytic properties and higher current density as its

'superaerophilic' architecture (Figure 5e). Notable ORR performance was obtained in a wide pH window (both in acid and base media, Figure 5f). Subsequently, PTFE treated CoNCNT carbon fiber paper showed superior stability at high current density (Figure 5g), attributed to the high surface area afforded by the morphology and excellent connectivity between the CoNCNT and carbon fibre substrate. Carbonisation of precursors based on metal-organic framework confined within crystal lattices has recently emerged as promising route of synthesising highly electroactive, defect and dopant rich materials.[78] Wang's group has used such approach, forming ZIF-8 in the presence of NaCl salt which was subsequently carbonised giving a 3-dimensional structure composed of linked defect rich, N-doped carbon polyhedron nanosheets. The electrocatalyst has shown comparative performance to a Pt based electrocatalysts, having a significantly higher performance than polyhedron carbon synthesised without the presence of salt. This has been ascribed to NaCl acting as a pore forming agent in addition to preserving the decomposed intermediate species resulting in significantly higher yield, number of defects and N-doping level.[78]

A summary of the fabrication and performance of the freestanding ORR electrocatalysts is presented in Table 2. The electrochemical characterization process of freestanding ORR electrocatalysts is still predominantly chosen to be conducted using the RDE method due to pre-existing lab equipment. However, the optimal structure of a free-standing electrode consists of porous hierarchical design and optimized surface chemistry to promote oxygen diffusion within the electrode and throughout its porous

structure, which would result in improvement of oxygen uptake and thus increasing the ORR performance.[13h, 25, 79]

3.3. ORR/OER bifunctional electrocatalysis

The lack of highly efficient, low cost and durable bifunctional electrocatalyst for both ORR and OER constitutes the main bottleneck for the development of cost-effective metal-air batteries and reversible fuel cells. Both ORR and OER have been identified to require different active sites in carbon materials and metal complexes. This poses a challenge for the simultaneous creation of both active sites, necessary for bifunctional activity. Many activity descriptors for electroactive materials can be represented as the so-called volcano plots, with compositions with optimal adsorbate binding strength or location of d-band centre represented at the top, corresponding to the highest performance.[80] These volcano plots further exemplify the differences in favourable adsorption features for OER and ORR.

Several strategies have been proposed for the design of ORR/OER bifunctional catalysts:

i) Formation of active sites designated separately to catalyse ORR and OER; an example of such approach includes a metal complex electrocatalysts typically utilizing transition metal ions like Co ions and Mn ions.[81]

ii) Alternatively, a composite material is created with one phase showing activity towards the ORR and another being electroactive towards OER.

iii) Creation of multiple active sites through a single process. A typical example are carbon materials, in which active sites for both ORR and OER can be formed by heteroatoms doping executed by methods such as hydrothermal treatment, plasma treatment or pyrolysis with dopant atoms in a range of chemical environments.[82]

iv) Creation of bifunctional active sites which are active towards both OER and ORR. For example, transition metal perovskite-type materials, where catalysis of both ORR and OER occurs on a single active site.[83]

3.3.1. Transition metal-based bifunctional electrocatalysts

Transition metal compounds containing Co or Mn are often chosen for OER/ORR bifunctional electrocatalysis due their inherently high electroactivity and low cost.[84] Zhang *et al.* reported a novel fabrication strategy of freestanding bifunctional electrocatalyst which consisted of electrodepositing conductive polypyrrole fibers onto a carbon cloth substrate, followed by immersion for 12 h in cobalt nitrile and 2-methylimidazole, to deposit a zeolitic metal-organic framework (ZIF-67), designed to increase porosity and introduce cobalt into the structure. This was subsequently pyrolyzed to yield a pearl-like structure of Co_4N anchored on the nanofibers (**Figure 6**a).[16b] At an overpotential of 570 mA, the electrocatalyst produced a current density of 130 mA cm^{-2} and the ORR limited current density was around 20 mA cm^{-2}. The electrocatalyst was fabricated into a flexible electrode for Zn-air battery which attained

maximum power density of 174 mW cm^{-2}, and a charge/discharge voltage gap of 0.84 V at 10 mA cm^{-2}.

Other strategies included the growth of N-doped carbon nanotubes *via* first coating the Ni foam with Al and Co nanoplatelets hydrothermally, followed by pyrolysis in N_2 atmosphere in the presence of ZIF-67 precursor. The electrocatalyst produced 10 and 50 mA cm^{-2} at an overpotentials of 265 and 368 mV for OER, respectively, showing extraordinary performance amongst other freestanding electrocatalysts. The freestanding structure was used as air cathode of a Zn-air battery exhibiting with energy density: 382 Wh kg^{-1} and producing charge/discharge voltage gap of 0.96 V at 5 mA cm^{-2} current density. The superior performance could be attributed to the excellent contact between the Ni substrate and CNTs, hierarchical cactus-like morphology, affording high surface area and high inherent activity of N-doped CNTs.[85]

In a similar effort, Chen's group electrodeposited iron oxide on stainless steel substrate, to serve as nucleation sites for the growth of N-doped carbon nanotubes by CVD, followed by electrodeposition of Co_4N nanoplatelets and annealing. This resulted in a morphology resembling human hair arrays.[22] The electrocatalyst produced current densities of 10 mA cm^{-2} at overpotentials of 300 mV and 440 mV for OER and ORR, respectively, indicating a high electrocatalytic activity. The Zn-air battery assembled using the freestanding material achieved an impressive energy density value of 847.6

Wh kg^{-1} at 20 mA cm^{-2} current density, combined with excellent durability as indicated by no visible voltage loss over 500 h of cycling.

Whilst the fabrication strategies mentioned above demonstrated feasibility for fabrication of freestanding air electrodes, they usually involve multistep processes and utilize relatively expensive precursors for metal-organic frameworks, limiting their commercial feasibility and scalability.

3.3.2. Carbon-based bifunctional catalysts

In our previous work, we reported how active site engineering can lead to superior OER/ORR activity in carbon based graphitic materials.[82] Density functional theory (DFT) calculations identified the active sites for ORR and OER on graphene co-doped with P–N sites for OER and N-doped sites for ORR.[82] Recently, Wang *et al.* proposed an Ar-plasma etched carbon cloth (P-CC) as ORR/OER bifunctional catalyst and analysed the activity of oxygen-doping and defects by DFT calculations.[13g] As shown in **Figure 7**a, b, the surface of the carbon cloth exhibited exposed, rich, graphene-like carbon nanosheets. The modified surface provided higher ORR/OER activity than pristine carbon cloth while the internal part of the carbon cloth retained its conductivity, flexibility and mechanical strength (Figure 7c, d). DFT calculations demonstrated that defective graphene structure with COOH species and non-defective graphene with C=O species had lower overpotential, and that the active sites are on the positive-charged carbon atoms.[13g] Figure 7e, f show the ORR and OER volcano plots of different active

sites on graphene material, respectively. The ORR/OER bifunctional activity of a carbon nitride sponge doped with N, P and S heteroatoms was also investigated.[86] DFT calculations identified positive charged P^+ centers and carbon atoms adjacent to thiophene or benzothiadizole structures as active centers for ORR, whereas nitrogen and oxygen were responsible for the OER activity.[5f, 16a, 66a, 86-87] Qiao *et al.* proposed a carbon fiber paper supported P-doped carbon nitride as bifunctional ORR/OER catalyst. This was one of the earliest works reported on freestanding carbon materials applied in Zn-air batteries.[5f, 16a] P-doped carbon nitrides were grown *in situ* on carbon paper by assembly of melamine and ethylene diphosphonic acid. The *as*-obtained PCN-CFP showed good flexibility and porous surface (**Figure 8**a-c). LSV and Tafel plots demonstrated a superior bifunctional activity and higher stability (Figure 8d). When tested in a Zn-air battery configuration (Figure 8e), PCN-CFP exhibited better performance than carbon fiber paper supported Pt catalyst,[5f, 16a] with a current density of 20 mA cm^{-2} at 1.05 V during discharging and 2.46 V during charging. No obvious potential change was observed after 50 charge-discharge cycles. Other freestanding carbon materials reported as ORR/OER bifunctional catalysts included H2-etched carbon cloth and carbonized polyimide films showing acceptable performance.[5d, 16c, 88]

Flexible electronics devices including roll-up displays, bendable smart phones, implantable biosensors, wearable have emerged rapidly in the recent years, creating an acute demand for viable flexible electrodes.[81b, 89] Wang *et al*. synthesized a flexible freestanding nanoporous carbon fiber films (NCNF) electrodes and utilized them in

flexible Zn-air batteries (**Figure 9**a, b).[5d, 88] The configuration of the flexible solid-state Zn-air battery consisted of freestanding NCNF air-cathode, zinc foil anode, alkaline poly (vinyl alcohol) (PVA) gel electrolyte and nickel foam current collector (Figure 9c, d). The as-fabricated Zn-air battery showed good flexibility, showing no obvious changes on the charge-discharge curve when the device was bended to a large angle or folded back to front (Figure 9e, f). These results show great potential of freestanding ORR/OER catalysts towards metal-air battery powered wearable electronic devices. The summaries of the performances of both metal-based and carbon-based freestanding OER/ORR bifunctional catalysts are listed in Table 3 and 4. Table c3 shows the OER/ORR electrocatalytic performances while Table 4 presents the Zn-air battery performances.

4. Summary and outlook

Freestanding materials possess obvious advantages that make them ideal for oxygen electrocatalysis applications, these including high electrical conductivity, high loading amount of active materials and high stability compared to powdered catalysts. This is due to a greater choice of precursor combinations, nanostructure manipulation, processing techniques and lack of binders. Commercial metal foams, metal plates, carbon fibers, and laboratory-synthesized carbon frameworks are used as skeletons for freestanding oxygen electrocatalysts. As summarized in this review, freestanding catalysts can afford extremely high and stable current densities, attributed to the high

mass-loading of active sites and the integrated structure. Moreover, the monolithic structure of freestanding catalysts facilitates their applications in water-splitting devices and Zn-air batteries.

As a promising category of electrocatalysts, freestanding materials still need further research to improve their performance. Here are some specific points that should be considered in future studies:

i) For OER electrocatalysis, the corrosion of the catalyst material at high potential is a key factor that affects stability, especially for carbon materials. Carbon skeletons without enough strength may even collapse in the severe OER condition. ii) The pore structure design and interface engineering are of great significance in gas-involving reactions. For freestanding catalysts, usually without rotation to accelerate mass transport, the rapid release of oxygen during OER, and the formation of abundant tri-phase regions during ORR are required. iii) The use of freestanding materials is essentially a way to increase the quantity of active sites, and then promote the catalytic activity. The research on freestanding catalysts should be combined with studies on the intrinsic activity of active sites, which is especially important to OER/ORR bifunctional electrocatalysis.

The increasing demand for sustainable energy calls for green, renewable energy sources and corresponding energy devices. Freestanding catalysts for oxygen evolution and reduction reaction are expected to play an important role in the development of the

energy devices. We hope that this review could inspire more research to improve the performance of freestanding electrodes, making them more suitable to fit the demand for durable and efficient energy conversion devices.

Acknowledgement

R. Chen, J. Feng and M. Qiao thanks the China Scholarship Council (CSC) for partially support this project. A. Belen Jorge thanks the UK Engineering Physical Research Council and her EPSRC First Grant EP/P031323/1. M. M. Titirici and Q. Zhang acknowledge the Royal Society for an Advanced Newton Fellowship (Ref: NA140249) while M Titirici thanks EPSRC grants EP/R021554/1 and EP/N509899/1 for additional financial support.

Table 1. Summary of best performing sample from each presented reference in section 3.1 (OER), all potentials mentioned are vs RHE.

Ref	Main composition	Assembly process	OER electrolyte	Potential at 10 mA cm^{-2} current density of catalyst [V]	Potential at 10 mA cm^{-2} current density of IrO_2[V]	Stability of catalysts (current remaining)	Stability of IrO_2 (current remaining)	Name of the sample
[12b]	CoP/Ni	Electrodeposition	1.0 M KOH	1.52	1.52	91.5% after 32 h	53.4% after 32 h	CoP - MNA
[12h]	Ni–P/NiO(Ni(OH)x)	Phosphorization	1.0 M KOH	191@ η = 350 mV	/	100% up to 25h	/	porous Ni–P foam
[13f]	Carbon fiber paper/Ni-P	Electrodeposition & phosphorization	1.0 M KOH	50.4@ η = 300 mV	/	Almost 100% for 180 h	/	CP@Ni-P
[56]	$Fe(PO_3)_2$ Ni_2P/Ni	Phosphorization	0.1 M KOH	1.45	1.53	Almost 100% for 20h	/	$Fe(PO_3)_2$
[28a]	N,O-dual doped graphene-CNT	Layer-by-layer assembly	0.1 M KOH	1.71*	1.81*	>80% after 5000s	/	NG-CNT
[69]	Nitrogen and sulfur codoped graphite	Oxidation followed by hydrothermal doping	0.1 M KOH	1.61	NA	77% after 60h	/	NSGF
[55]	NiFe LDH	Hydrothermal deposition	0.1 M KOH	1.48	1.59 (Ir/C)	93.6% for 10 h at 1.52 V	79.6% for 10 h at 1.61 V (Ir/C)	NiFe-LDH
[12g]	NiFe LDH	Hydrothermal deposition	0.1 M KOH	1.55	/	92% for 8000 s at 10 mA cm^{-2}	/	LDH/G/Ni
[12i]	NiCoFe LDH	Electrodeposition	0.1 M KOH	1.50	/	/	/	$Ni_{2.5}Co_{0.5}Fe$/NF
[12k]	$LaCo_{0.8}Fe_{0.2}O_3$ perovskite	Electrodeposition	0.1 M KOH	1.58	/	100% for 10000 s at 2.0 mA cm^{-2}	/	NF/LCFO-Ar

[54b]	Ni_3S_2	Hydrothermal deposition	0.1 M KOH	1.41	/	95% for 10 h	/	Ni_3S_2/Ni
[9]	$NiCo_2S_4$	Hydrothermal deposition	1.0 M KOH	1.49	1.57	85% for 50 h at 1.527 V	/	$NiCo_2S_4$ NW/NF
[54a]	Fe- and O- doped Co_2P	Chemical vapor deposition	1.0 M KOH	1.50	1.58	85% for 100 h	/	CoFePO
[12f]	Co_9S_8	Hydrothermal deposition	1.0 M KOH	1.58	/	No obvious potential change for 50 h at 20 mA cm^{-2}	/	Co@Co_9S_8-180
[12e]	CoP	Chemical vapor deposition	1.0 M KOH	1.48	1.55 (RuO_2)	Stable potential for 24 h at 50 mA cm^{-2}	/	CoP NWs
[12a]	NiFe oxide	Galvanic replacement reaction	1.0 M KOH	1.45 (5 mA cm^{-2})	/	Stable current density for 10 h at 1.71 V in 10 M KOH	/	$NiFeO_x$
[60]	NiFe hydroxide	Hydrothermal deposition	1.0 M KOH	1.55 (20 mA cm^{-2})	/	93% after 4000 cycles	/	SSNNi
[61]	Co_2P	Calcination	1.0 M KOH	1.55	1.58*	70% for 12 h at 1.55 V	/	Co_2P/Co-Foil
[62]	Fe-Ni sulfide	Hydrothermal deposition	1.0 M KOH	1.51	1.57	~97% for 9 h at 1.56 V	/	Fe-Ni_3S_2/FeNi
[13l]	$NiCo_2O_4$	Hydrothermal and electrochemical deposition	1.0 M NaOH	1.55	1.57	No obvious change in LSV plot after 30 h	/	$NiCo_2O_4$ core-shell
[63b]	Nickel borate	Electrochemical deposition	0.1 M KBi	1.70	1.61 (RuO_2)	Stable after 25 h	/	Ni-Bi/CC
[13k]	Co-ZnO	Hydrothermal deposition	0.1 M KOH	1.59	1.58 (Ir/C)	/	/	ZCO/CF

[63a]	Co_4N	Chemical vapor deposition	1.0 M KOH	1.49	/	98% for 12 h at 1.55 V	/	Co_4N/CC
[59]	Phosphorus doped Co_3O_4	Electrodeposition	1.0 M KOH	1.51	/	/	/	P-Co_3O_4
[44b]	$Ni_xFe_{1-x}Se$ shell Ni(Fe)OOH core	Hydrothermal deposition	1.0 M KOH	1.49 (100 mA cm^{-2})	1.54 (100 mA cm^{-2})	Insignificant change after 2000 CV cycles	/	$Ni_xFe_{1-x}Se$@Ni(Fe)OOH

* Values estimated from LSV graphs (unless otherwise noted at 1600rpm);

/ no information given

Potentials were converted as follows:

$E_{RHE} = E_{Ag/AgCl} + E^0_{Ag/AgCl} + 0.0591 \times pH$

$E_{RHE} = E_{Hg/HgO} + E^0_{Hg/HgO} + 0.0591 \times pH$

Table 2. Summary of best performing sample from each presented reference in section 3.2 (ORR), all potentials mentioned are vs RHE.

Ref	Main composition	Assembly process	ORR electrolyte	Onset potential of catalyst [V]	Onset potential of Pt standard [V]	Limiting current density of catalyst at 0.4 V	Limiting current density of Pt at 0.4 V	Stability (current remaining)	Name of the sample
[75]	N-doped carbon nanofiber	Electrospinning	0.1M KOH	0.946*	0.991*	-3.2*(mA cm^{-2})	-4.8*(mA cm^{-2})	94% after 10000s	NCNFs
[13h]	Co-N doped CNT grow on CFP with PTFE treated	Solvothermal; in-situ growth under 600 °C	0.1M/1.0M /6.0M KOH 0.1M/0.5M /1.0M H_2SO_4	0.85/0.82/0.9 0.8/0.71/0.78*	1/0.99/0.98 0.88/0.8/0.8 8*	-20/-70/-155 -30/-40/-60* (mA cm^{-2})	-30/-80/-140 -35/-60/-75* (mA cm^{-2})	160 mA cm^{-2} (~99%) After 20h	PTFE-CoN CNT-CFP
[17]	n-doped carbon flake fragments present on the walls of the CNT	CVD; PECVD; carbonization	0.1M KOH	0.79*	0.99*	-36*(mA cm^{-2}) vs. Ag/AgCl	-43*(mA cm^{-2}) vs. Ag/AgCl	90% after 20000s	N-VA-CNTs/GF

* Values estimated from LSV graphs (unless otherwise noted at 1600rpm);

/ no information given

Potentials were converted as follows:

$E_{RHE} = E_{Ag/AgCl} + E^0_{Ag/AgCl} + 0.0591 \times pH$

$E_{RHE} = E_{Hg/HgO} + E^0_{Hg/HgO} + 0.0591 \times pH$

Table 3. Summary of best performing sample from each presented reference in section 3.3 (ORR+OER bifunctional), all potentials mentioned are vs RHE.

Ref	Active material	Assembly process	Electrolyte	Potential at 10 mA cm^2 OER current density (E_{10}) of catalyst[V]	Potential at 10 mA cm^{-2} OER current density (E_{10}) of IrO_2[V]	ORR half-wave potential ($E_{1/2}$) of catalyst (V)	ORR half-wave potential ($E_{1/2}$) of Pt (V)	Potential gap between E_{10} and $E_{1/2}$ of catalyst (V)	OER stability	ORR stability	Name of the sample
[16a]	Phosphorus-doped graphitic carbon nitrides	Growing active materials on carbon fiber paper	0.1 M KOH	1.63	/	0.67	0.80	0.96	93.4% current density remaining after 30 h at 1.63 V	97.8% current density remaining after 30 h at 0.40 V	PCN-NFP
[22]	Co_3O_4 and nitrogen-doped carbon nanotube	Growing active materials on stainless steel mesh fibers	0.1 M KOH	1.53	1.55 (Ir/C)	0.80* (0.79 for 10 mA cm^{-2} ORR current density)	0.79* (0.71 for 10 mA cm^{-2} ORR current density)	0.73	30 mV overpotential increase after 7 h at 10 mA cm^{-2}	15 mV overpotential increase after 7 h at 10 mA cm^{-2}	Co_3O_4-NCNT/SS
[90]	N-doped carbon material	Pyrolyzing facial cotton	0.1 M KOH	1.52	1.62 (Ir/C)	0.71	0.83	0.81	/	72.9% current density remaining after 100 h	NCMT-1000 (3D)

[88] (RDE)	N-doped carbon material	Pyrolyzing polyimide film	0.1 M KOH	1.84	1.58	0.82	0.83	1.02	/	/	NCNF-1000
[16b]	Co_4N and Co-N-C	Growing active materials on carbon cloth	1.0 M KOH	1.54	1.54 (RuO_2)	0.80	0.63	0.74	~98% current density remaining after 20 h at 1.54 V	~98% current density remaining after 20 h at 0.50 V	Co_4N/CNW/CC
[12j]	N-doped carbon nanotube	Growing CNTs on layered double hydroxide supported on Ni foam	0.1 M KOH	1.65	/	0.81	0.82*	0.84	No obvious change in current density after 10 times of switch (5000 s) between ORR (0.6 V) and OER (1.6 V)		3D NCNT array
[13g]	Edge-rich oxygen-doped graphene material	Ar plasma treating of carbon cloth	1.0 M KOH	1.68	/	0.64*	/	1.04	~91% current density remaining after 40000 s at initial current density of 5 mA cm^{-2}	/	P-CC
[16c]	Defect-rich porous graphene material	High temperature H_2 etching of carbon fibers	0.1 M KOH	1.62	/	0.61	/	1.01	Insignificant change after 900 cycles (9h) between 0.0-1.8V		o-CC-H_2

* Values estimated from LSV graphs;

/ no information given

Table 4. Summary of Zn-air battery performances of best performing sample from each presented reference in section 3.3 (ORR+OER bifunctional).

Ref	Active material	Catalyst assembly process	Electrolyte	Open circuit voltage (V)	Discharge voltage (V)	Maximum power density (mW cm^{-2})	Capacity (mAh g^{-1})	Charge/discharge voltage gap (V)	Charge/discharge stability	Name of sample
[16a]	Phosphorus-doped graphitic carbon nitrides	Growing active materials on carbon fiber paper	6.0 M KOH	/	1.05 (20 mA cm^{-2})	/	/	1.41 (20 mA cm^{-2})	20 mA cm^{-2} 50 cycles 500 min No obvious change	PCN-NFP
[22]	Co_3O_4 and nitrogen-doped carbon nanotube	Growing active materials on stainless steel mesh fibers	Cellulose film gelled with 6.0 M KOH (flexible)	1.42*	1.36* (5 mA cm^{-2}) 1.14* (50 mA cm^{-2})	160.7	652.6 (5 mA cm^{-2}) 632.3 (50 mA cm^{-2})	0.79* (25 mA cm^{-2})	25 mA cm^{-2} Over 600 h No obvious change	Co_3O_4-NCNT/SS
[88]	N-doped carbon material	Pyrolyzing polyimide film	6.0 M KOH + 0.2 M ZnAc	1.48	1.27 (5 mA cm^{-2}) 1.24 (10 mA cm^{-2})	185	660 (5 mA cm^{-2}) 626 (10 mA cm^{-2})	0.73 (10 mA cm^{-2})	10 mA cm^{-2} 500 cycles 83 h 0.13 V increase of voltage gap	NCNF-1000
			Alkaline poly(vinyl	1.26	1.0 (2 mA cm^{-2})	/	378	0.78 (2 mA cm^{-2})	2 mA cm^{-2} 48 cycles	

			alcohol) (PVA) gel (flexible)				(2 mA cm^{-2})		6h No obvious change	
[16b]	Co_4N and Co-N-C	Growing active materials on carbon cloth	6.0 M KOH + 0.2 M ZnAc	~1.4	/	174	774 (10 mA cm^{-2})	0.84 (10 mA cm^{-2})	10 mA cm^{-2} 408 cycles 136 h	Co_4N/CNW/CC
							701 (50 mA cm^{-2})	1.09 (50 mA cm^{-2})	No obvious change	
			Alkaline PVA gel (cable-type, flexible)	1.346	1.23 (0.5 mA cm^{-2})	/	/	0.78* (0.5 mA cm^{-2}) 1.02* (1 mA cm^{-2})	0.5 and 1 mA cm^{-2} 36 cycles 12 h No obvious change	
[12j]	N-doped carbon nanotube	Growing CNTs on layered double hydroxide supported on Ni foam	6.0 M KOH + 0.2 M ZnAc	1.47	1.31 (2 mA cm^{-2}) 1.26 (5 mA cm^{-2}) 1.22 (10 mA cm^{-2}) 1.13 (25 mA cm^{-2}) 1.01 (50 mA cm^{-2})	190	623.4 (5 mA cm^{-2})	0.75 (10 mA cm^{-2}) 0.88 (25 mA cm^{-2})	/	3D NCNT array
			Alkaline PVA gel (flexible)	/	1.02 (5 mA cm^{-2})	/	356 (5 mA cm^{-2})	0.96 (5 mA cm^{-2})	/	

[16c]	Defect-rich porous graphene material	High temperature H_2 etching of carbon fibers	6.0 M KOH + 0.2 M $ZnCl_2$	/	1.08 (2 mA cm^{-2})	91.4	707 (20 mA cm^{-2})	0.92 (2 mA cm^{-2})	2 mA cm^{-2} 80 cycles 26h No obvious change	o-CC-H_2
			Alkaline PVA gel (flexible)	1.258	1.04 (1 mA cm^{-2})	/	/	0.97 (1 mA cm^{-2})	1 mA cm^{-2} 40 cycles 80 min 0.09 V increase of voltage gap	

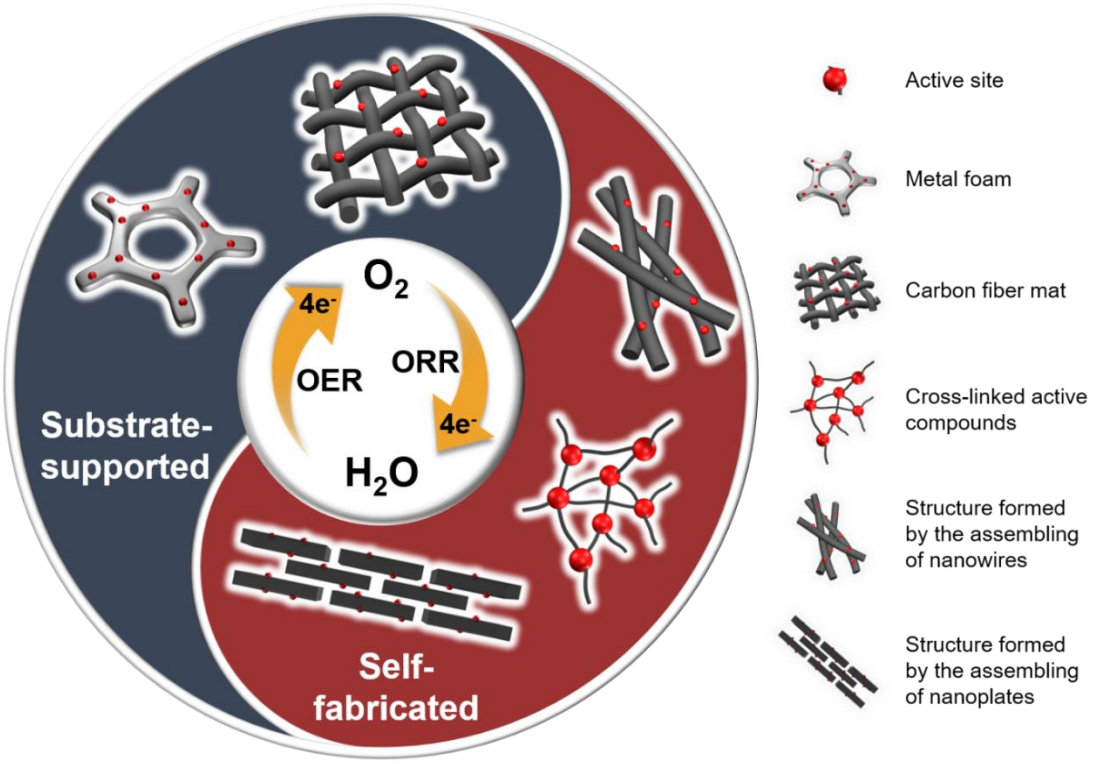

Scheme 1. Freestanding catalysts for oxygen electrocatalysis. Two categories of freestanding catalysts, substrate-supported and self-fabricated catalysts, are presented here.

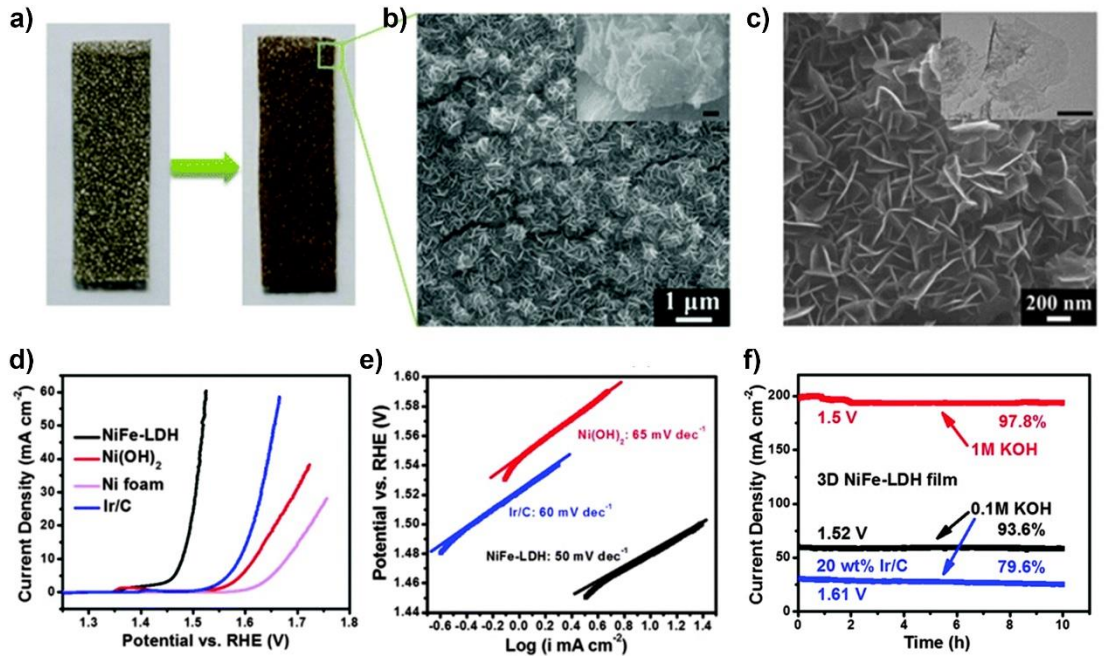

Figure 1. a) Optical images of Ni foams before (left) and after (right) the deposition of NiFe LDH. b) and c) Low- and high-magnification SEM images of NiFe LDH nanosheets deposited on Ni foam. Inset: cross-view SEM image and typical TEM image, scale bar: 100 nm. d) LSV plots and e) Tafel plots of various catalysts. The electrochemical tests were performed in O_2-saturated 0.10 M KOH electrolyte. f) Stability test of 3D NiFe LDH film deposited on Ni foam and Ir/C loaded on Ni foam with the same loading amount as NiFe LDH.[55] Reproduced with permission from Ref 55. Copyright 2014 Royal Society of Chemistry.

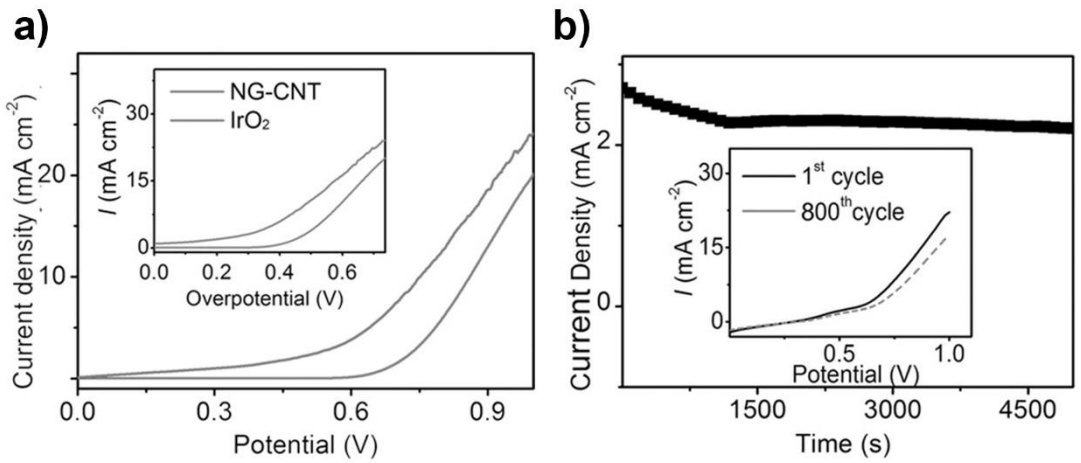

Figure 2. a) Oxygen electrochemical catalysis on NG-CNT in 0.1 M KOH electrolyte: LSV plots in comparison with IrO_2 collected at 30 mV s^{-1}; *inset*: corresponding data re-plotted as the current density vs. overpotential. b) Chronoamperometric response at 0.55 V vs. Ag/AgCl; *inset*: LSV plots for the 1st and 800th potential cycles.[28a] Reproduced with permission from Ref 28a. Copyright 2014 John Wiley and Sons.

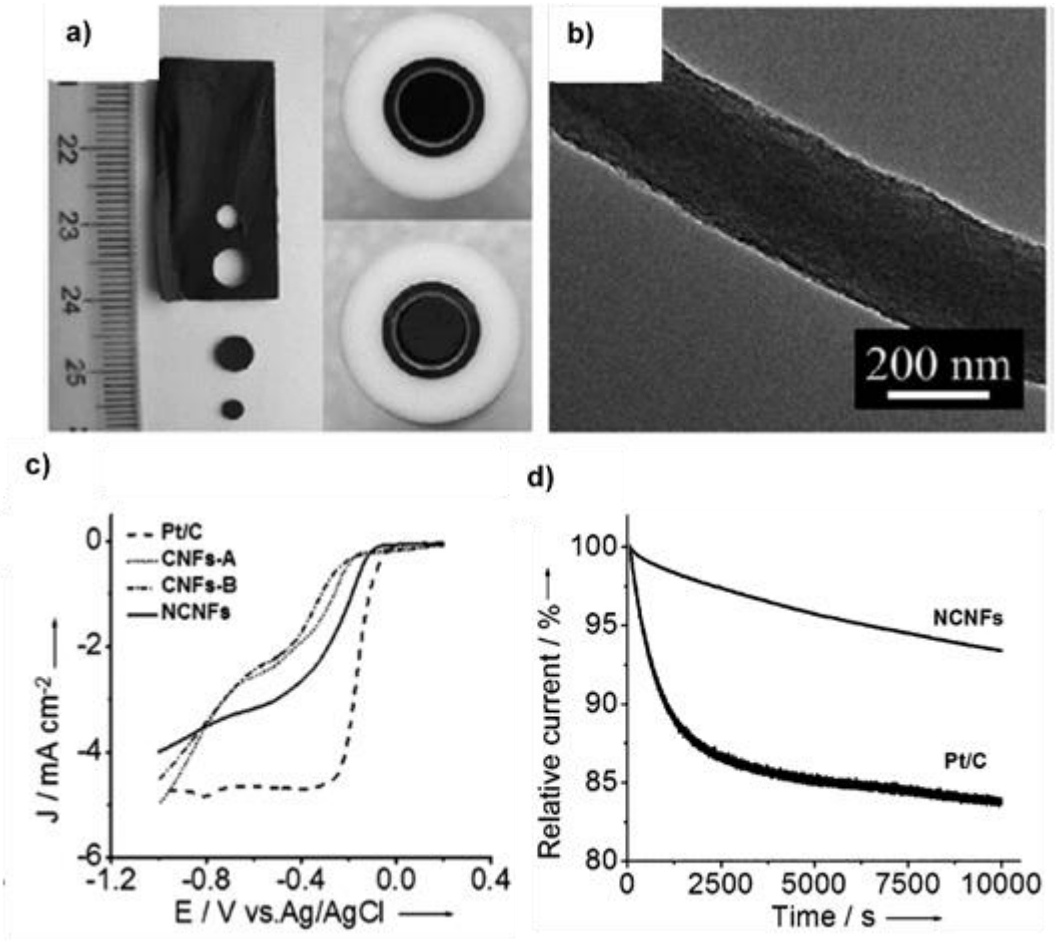

Figure 3. a) Photograph of free-standing films and disk-shaped N-CNF for modification of the electrode. b) TEM images of N-CNF. c) LSV for ORR testing of N-CNF and Pt/C in O_2-saturated 0.1M KOH solution at 10 mVs^{-1} scan rates at 1600rpm rotation rate. d) Chronoamperometric response of N-CNF and Pt/C at -0.26 V in O_2-saturated 0.1M KOH at 1600rpm rotation rate.[75] Reproduced with permission from Ref 75. Copyright 2013 Royal Society of Chemistry.

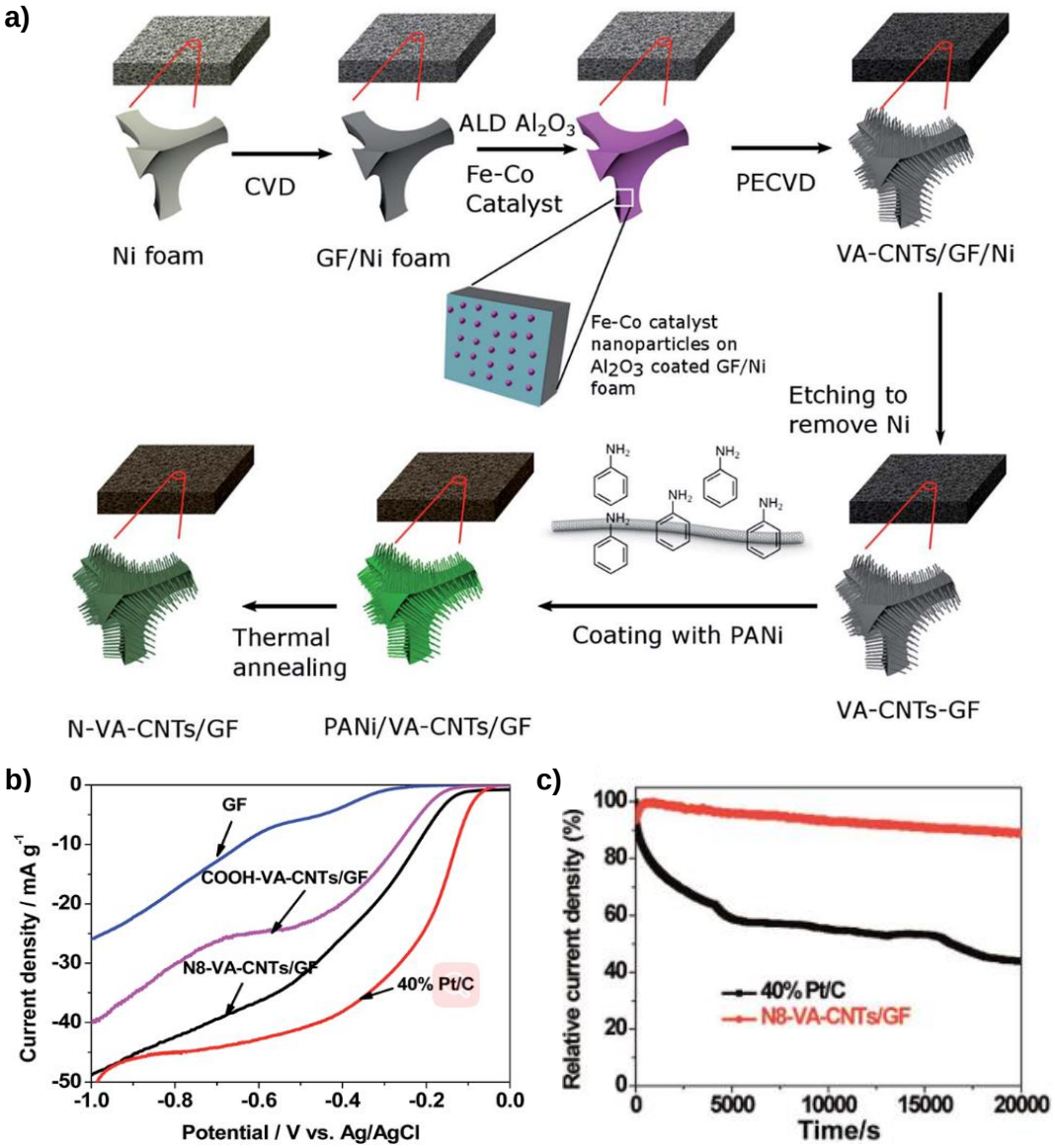

Figure 4. a) Synthesis route of N-VA-CNTs/GF. b) LSV curves of graphene foam (GF), 800°C treated N-doped vertically aligned carbon nanotubes supported by graphene foam (N8-VA-CNTs/GF), undoped VA-CNTs/GF (COOH-VA-CNTs/GF) and commercial 40wt% Pt/C catalyst. c) Durability evaluation of N8-VA-CNTs/GF and 40% Pt/C for 20000s.[17] Reproduced with permission from Ref 17. Copyright 2017 Royal Society of Chemistry.

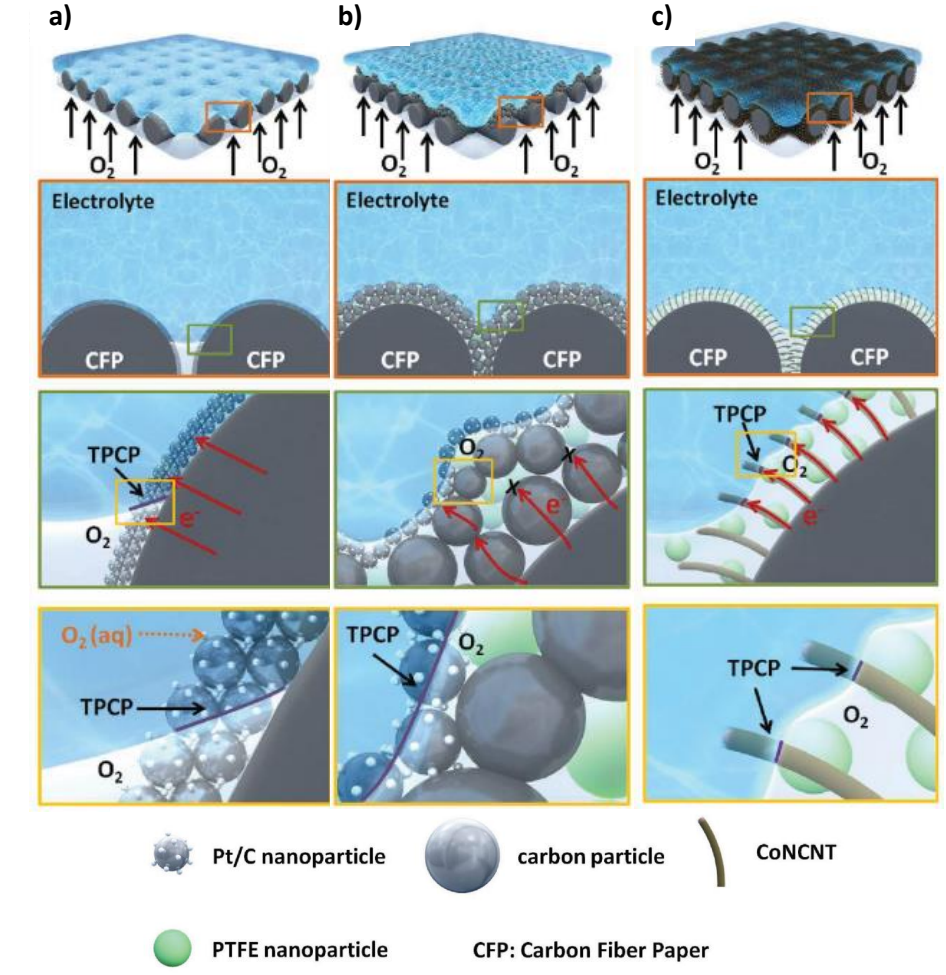
a)
b)
c)
Electrolyte
CFP
TPCP
e⁻
Pt/C nanoparticle
carbon particle
CoNCNT
PTFE nanoparticle
CFP: Carbon Fiber Paper

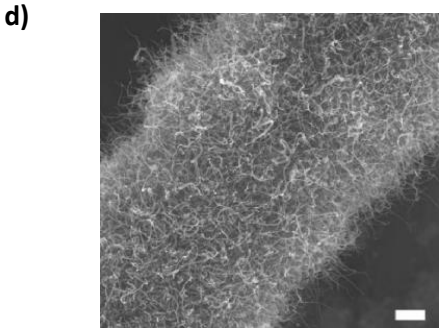
d)

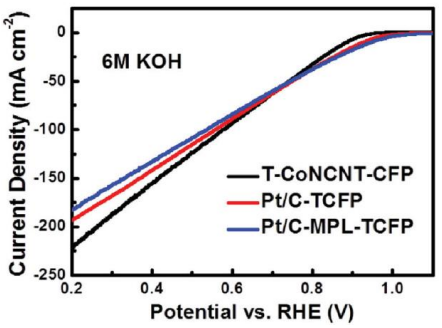
e)
6M KOH
Current Density (mA cm⁻²)
Potential vs. RHE (V)
T-CoNCNT-CFP
Pt/C-TCFP
Pt/C-MPL-TCFP

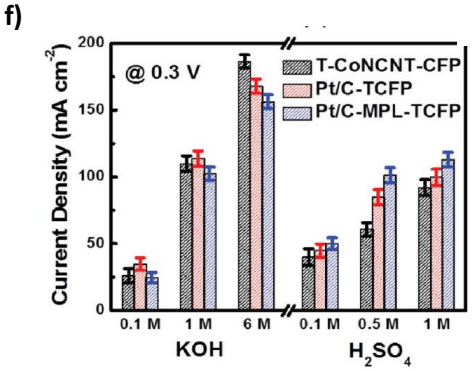
f)
@ 0.3 V
Current Density (mA cm⁻²)
T-CoNCNT-CFP
Pt/C-TCFP
Pt/C-MPL-TCFP
0.1 M
1 M
6 M
KOH
0.1 M
0.5 M
1 M
H2SO4

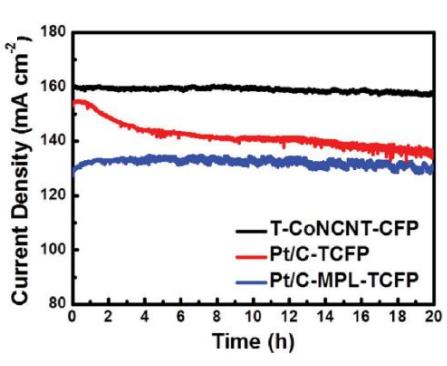
g)
Current Density (mA cm⁻²)
Time (h)
T-CoNCNT-CFP
Pt/C-TCFP
Pt/C-MPL-TCFP

Figure 5. Schematic illustration of a) commercial Teflon-treated carbon paper with Pt/C catalyst (Pt/C-TCFP) under electrolyte, b) commercial air electrode with an additional MPL located between TCFP and Pt/C catalyst (Pt/C-MPL-TCFP), c) 'superaerophilic' structured electrode. d) SEM image of CoNCNT arrays on CFP (scale bar is 2μm). e) ORR polarization of the three electrodes showed in (a-c) in oxygen bubbled 6M KOH solution. f) ORR current density of the three electrodes at 0.3V in both basic and acidic solution. g) Chronoamperometric response for the three electrodes.[13h] Reproduced with permission from Ref 13h. Copyright 2016 John Wiley and Sons.

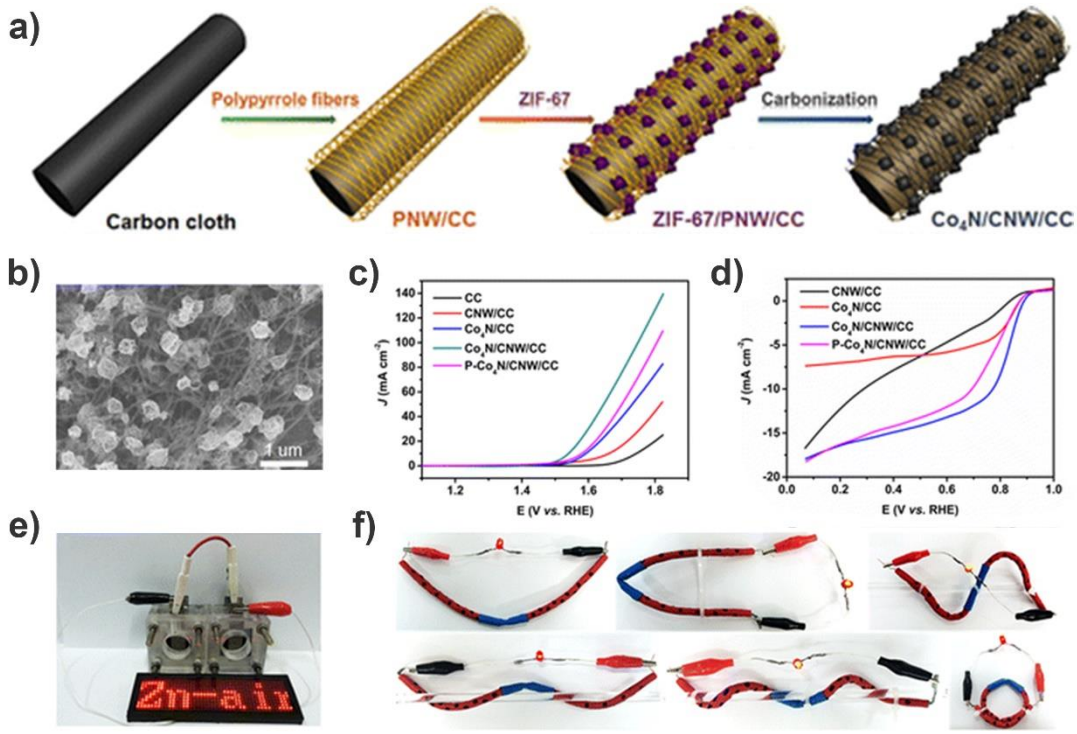

Figure 6. a) Schematic representation of the synthesis of Co_4N/CNW/CC. b) SEM image of Co_4N/CNW/CC. LSV curves for c) OER and d) ORR at a scan rate of 5 mV s^{-1} in 1 M KOH of Co_4N/CNW/CC. Photograph of e) conventional Zn-air battery and f) flexible Zn-air batteries with Co_4N/CNW/CC as air cathode.[16b] Reproduced with permission from Ref 16b. Copyright 2016 American Chemical Society.

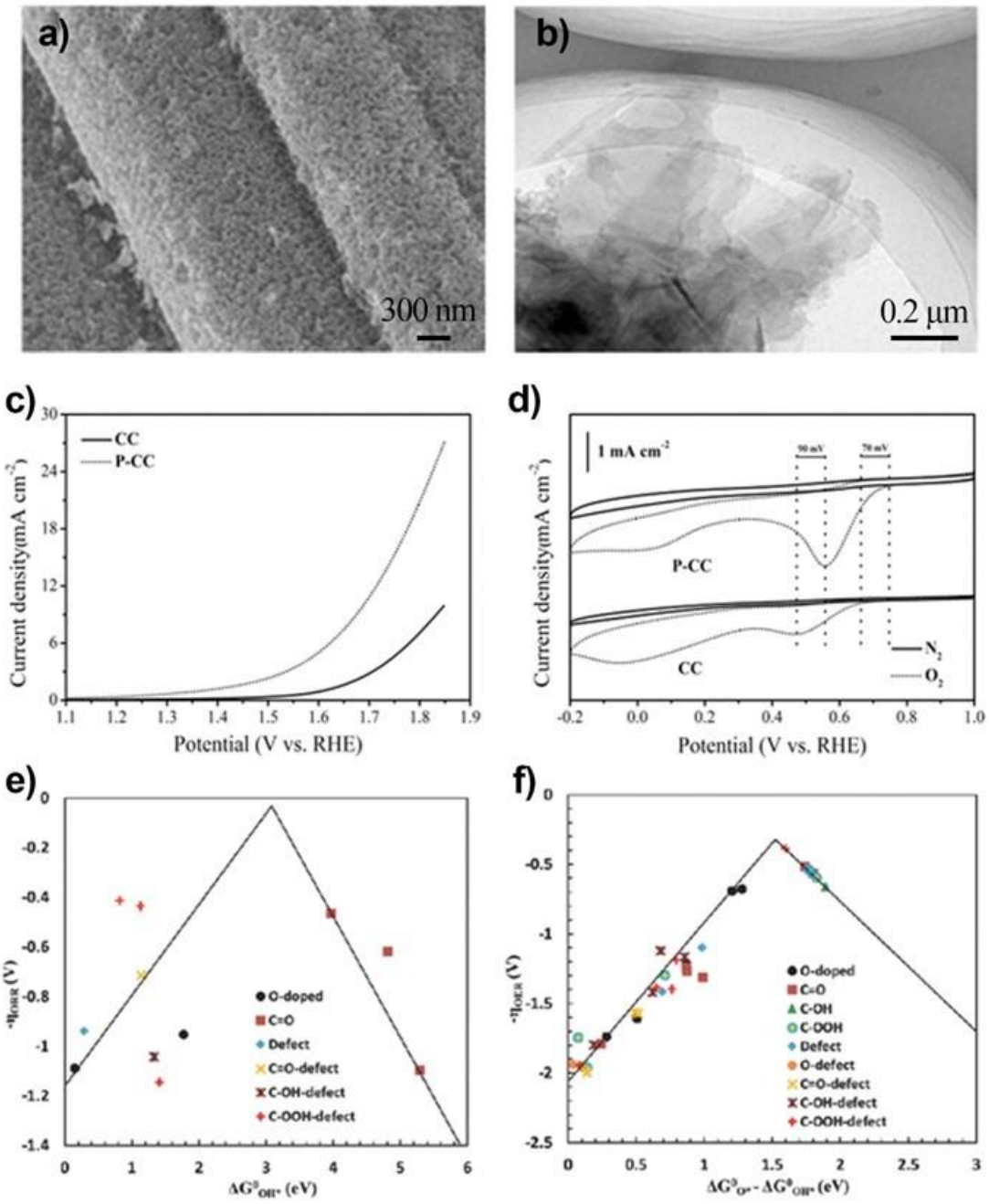

Figure 7. a) SEM image of P-CC. b) TEM image of P-CC. c) LSV curves of CC and P-CC for OER at 5 mV s^{-1} scan rate in 1.0 M KOH. d) Cyclic voltammograms (CV) of CC and P-CC for ORR at 50 mV s^{-1} scan rate in both N_2 and O_2-saturated 0.1 M KOH. Volcano plots for e) ORR and f) OER on different sites of armchair and zigzag graphene

nanoribbons.[13g] Reproduced with permission from Ref 13g. Copyright 2017 John Wiley and Sons.

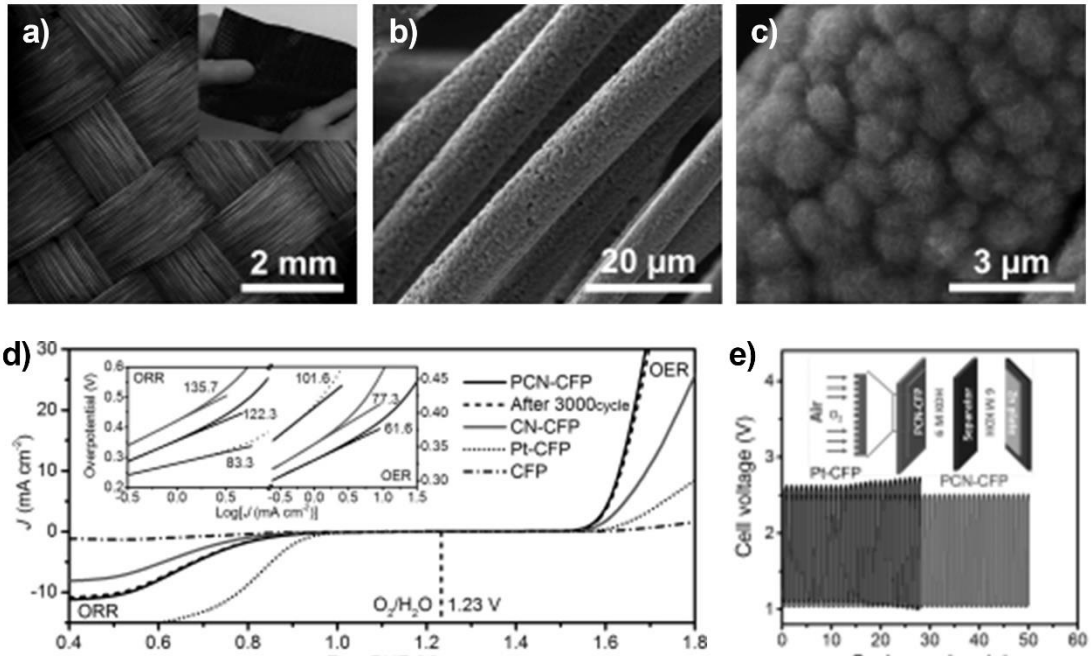

Figure 8. a-c) SEM images of PCN-CFP (*Inset* (a): photograph of PCN-CFP). d) LSV of PCN-CFP, CN-CFP, Pt-CFP and CFP in O_2-saturated 0.1 M KOH solution at 0.5 mV s^{-1} scan rate (*Inset*: Tafel plots of PCN-CFP, CN-CFP and Pt-CFP). e) Charge-discharge cycling curves using PCN-CFP and Pt-CFP directly as the air cathodes (*Inset*: schematic configuration of Zn-air batteries).[16a] Reproduced with permission from Ref 16a. Copyright 2015 John Wiley and Sons.

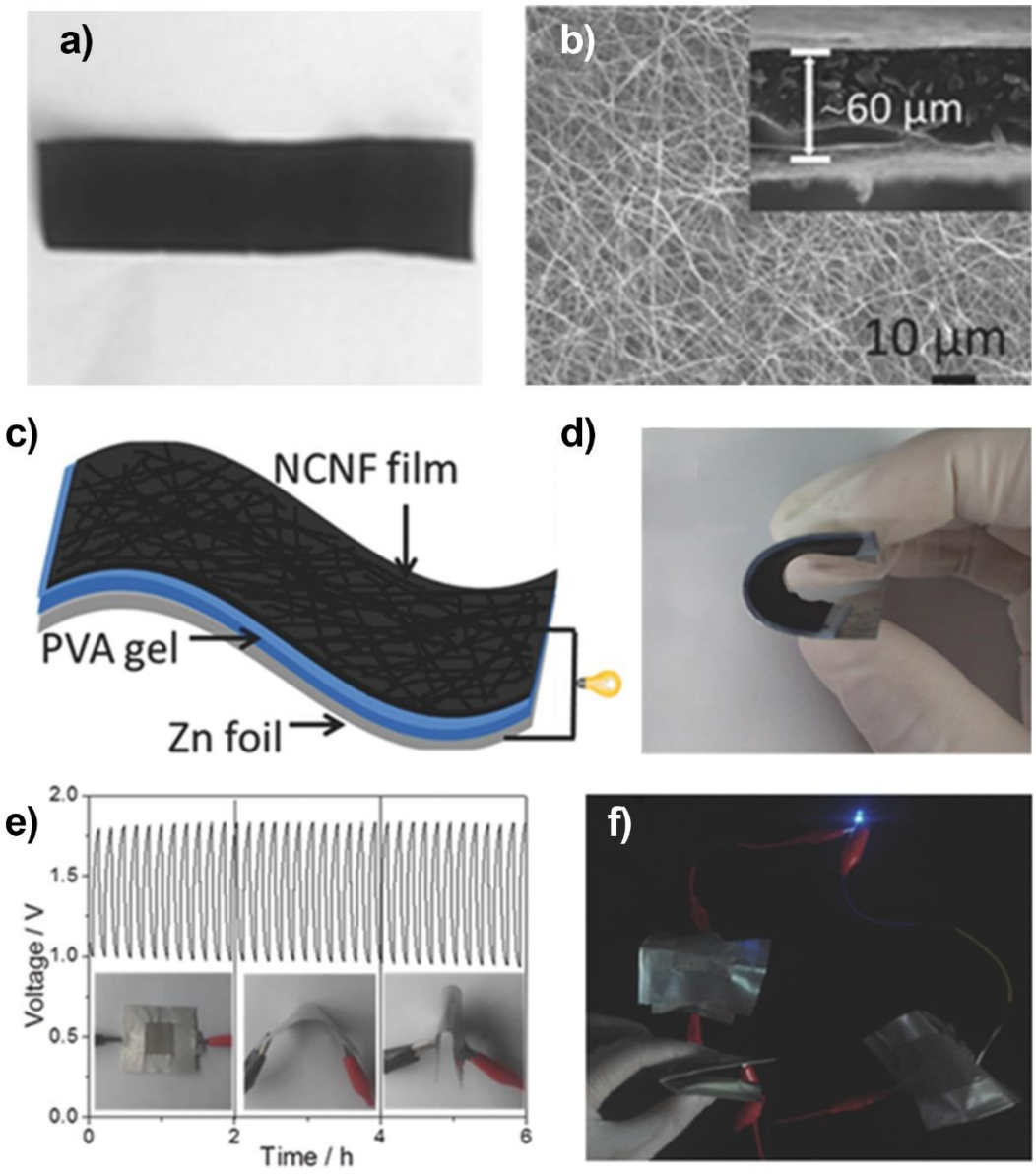

Figure 9. a) Photograph of flexible NCNF. b) SEM images of NCNF. c) Schematic representation and d) photograph of the all-solid-state rechargeable Zn-air battery. e) Galvanostatic discharge-charge cycling curve at 2 mA cm^{-2} for the all-solid-state rechargeable Zn-air battery with NCNF-1000 as catalyst, applying bending strain every 2 h. f) Photograph of a blue LED (≈3.0 V) powered by three all-solid-state Zn-air

batteries in series.[88] Reproduced with permission from Ref 88. Copyright 2016 John Wiley and Sons.

[1] aJ. P. Lai, A. Nsabimana, R. Luque, G. B. Xu, *Joule* **2018**, *2*, 76-93; bC. R. Raj, A. Samanta, S. H. Noh, S. Mondal, T. Okajima, T. Ohsaka, *J. Mater. Chem. A* **2016**, *4*, 11156-11178; cX. Liu, L. Dai, *Nat. Rev. Mater.* **2016**, *1*, 16064.

[2] C. L. Zhang, X. C. Shen, Y. B. Pan, Z. M. Peng, *Front. Energy* **2017**, *11*, 268-285.

[3] aT. Reier, M. Oezaslan, P. Strasser, *ACS Catal.* **2012**, *2*, 1765-1772; bU. A. Paulus, T. J. Schmidt, H. A. Gasteiger, R. J. Behm, *J. Electroanal. Chem.* **2001**, *495*, 134-145; cY. Lee, J. Suntivich, K. J. May, E. E. Perry, Y. Shao-Horn, *J. Phys. Chem. Lett.* **2012**, *3*, 399-404.

[4] R. Bashyam, P. Zelenay, *Nature* **2006**, *443*, 63-66.

[5] aS. Anantharaj, S. R. Ede, K. Sakthikumar, K. Karthick, S. Mishra, S. Kundu, *ACS Catal.* **2016**, *6*, 8069-8097; bL. Han, S. J. Dong, E. K. Wang, *Adv. Mater.* **2016**, *28*, 9266-9291; cC. Tang, Q. Zhang, *Adv. Mater.* **2016**, *29*, 1604103; dJ. H. Wang, W. Cui, Q. Liu, Z. C. Xing, A. M. Asiri, X. P. Sun, *Adv. Mater.* **2016**, *28*, 215-230; eL. G. Feng, H. G. Xue, *ChemElectroChem* **2017**, *4*, 20-34; fJ. R. Galan-Mascaros, *ChemElectroChem* **2015**, *2*, 37-50; gD. S. Su, S. Perathoner, G. Centi, *Chem. Rev.* **2013**, *113*, 5782-5816; hZ. W. Chen, D. Higgins, A. P. Yu, L. Zhang, J. J. Zhang, *Energy Environ. Sci.* **2011**, *4*, 3167-3192; iD. W. Wang, D. S. Su, *Energy Environ. Sci.* **2014**, *7*, 576-591; jC. Tang, M. M. Titirici, Q. Zhang, *J. Energy Chem.* **2017**, *26*, 1077-1093; kC. Tang, H. F. Wang, X. L. Zhu, B. Q. Li, Q. Zhang, *Part. Part. Syst. Char.* **2016**, *33*, 473-486; lZ. Q. Zhou, N. Mahmood, Y. C. Zhang, L. Pan, L. Wang, X. W. Zhang, J. J. Zou, *J. Energy Chem.* **2017**, *26*, 1223-1230; mB. Q. Li, Z. J. Xia, B. S. Zhang, C. Tang, H. F. Wang, Q. Zhang, *Nat. Commun.* **2017**, *8*, 934.

[6] T. Y. Ma, S. Dai, S. Z. Qiao, *Mater. Today* **2016**, *19*, 265-273.

[7] X. Y. Lu, C. A. Zhao, *Nat. Commun.* **2015**, *6*, 6616.

[8] Y. G. Li, H. J. Dai, *Chem. Soc. Rev.* **2014**, *43*, 5257-5275.

[9] A. Sivanantham, P. Ganesan, S. Shanmugam, *Adv. Funct. Mater.* **2016**, *26*, 4661-4672.

[10] aH. J. Qiu, Y. X. Guan, P. Luo, Y. Wang, *Biosens. Bioelectron.* **2017**, *89*, 85-95; bS. Nardecchia, D. Carriazo, M. L. Ferrer, M. C. Gutierrez, F. del Monte, *Chem. Soc. Rev.* **2013**, *42*, 794-830; cC. G. Palivan, R. Goers, A. Najer, X. Y. Zhang, A. Car, W. Meier, *Chem. Soc. Rev.* **2016**, *45*, 377-411; dO. Shekhah, J. Liu, R. A. Fischer, C. Woll, *Chem. Soc. Rev.* **2011**, *40*, 1081-1106; eX. D. Zhang, Y. Xie, *Chem. Soc. Rev.* **2013**, *42*, 8187-8199; fQ. Y. Liao, S. X. Jin, C. X. Wang, *J.*

Materiomics **2016**, *2*, 291-308; gJ. Di, J. X. Xia, H. M. Li, Z. Liu, *Nano Energy* **2017**, *35*, 79-91; hS. J. Peng, L. L. Li, J. K. Y. Lee, L. L. Tian, M. Srinivasan, S. Adams, S. Ramakrishna, *Nano Energy* **2016**, *22*, 361-395; iX. N. Zhao, P. P. Zhang, Y. T. Chen, Z. Q. Su, G. Wei, *Nanoscale* **2015**, *7*, 5080-5093; jT. Fujie, *Polym. J.* **2016**, *48*, 773-780.

[11] C. Tang, H. F. Wang, Q. Zhang, *Accounts. Chem. Res.* **2018**, *doi: 10.1021/acs.accounts.7b00616*.

[12] aJ. Y. Wang, L. L. Ji, S. S. Zuo, Z. F. Chen, *Adv. Energy Mater.* **2017**, *7*, 1700107; bY. P. Zhu, Y. P. Liu, T. Z. Ren, Z. Y. Yuan, *Adv. Funct. Mater.* **2015**, *25*, 7337-7347; cC. Tang, R. Zhang, W. B. Lu, L. B. He, X. Jiang, A. M. Asiri, X. P. Sun, *Adv. Mater.* **2017**, *29*, 1602441; dX. Zou, Y. P. Liu, G. D. Li, Y. Y. Wu, D. P. Liu, W. Li, H. W. Li, D. J. Wang, Y. Zhang, X. X. Zou, *Adv. Mater.* **2017**, *29*, 1700404; eW. Li, X. F. Gao, D. H. Xiong, F. Xia, J. Liu, W. G. Song, J. Y. Xu, S. M. Thalluri, M. F. Cerqueira, X. L. Fu, L. F. Liu, *Chem. Sci.* **2017**, *8*, 2952-2958; fD. H. Xiong, Q. Q. Zhang, S. M. Thalluri, J. Y. Xu, W. Li, X. L. Fu, L. F. Liu, *Chem. Eur. J.* **2017**, *23*, 8749-8755; gH. F. Wang, C. Tang, Q. Zhang, *J. Mater. Chem. A* **2015**, *3*, 16183-16189; hX. G. Wang, W. Li, D. H. Xiong, L. F. Liu, *J. Mater. Chem. A* **2016**, *4*, 5639-5646; iX. L. Zhu, C. Tang, H. F. Wang, B. Q. Li, Q. Zhang, C. Y. Li, C. H. Yang, F. Wei, *J. Mater. Chem. A* **2016**, *4*, 7245-7250; jZ. H. Li, M. F. Shao, Q. H. Yang, Y. Tang, M. Wei, D. G. Evans, X. Duan, *Nano Energy* **2017**, *37*, 98-107; kB. Q. Li, C. Tang, H. F. Wang, X. L. Zhu, Q. Zhang, *Sci. Adv.* **2016**, *2*, e1600495; lJ. L. Liu, Y. Yang, B. Ni, H. Y. Li, X. Wang, *Small* **2017**, *13*, 1602637.

[13] aG. J. He, M. Qiao, W. Y. Li, Y. Lu, T. T. Zhao, R. J. Zou, B. Li, J. A. Darr, J. Q. Hu, M. M. Titirici, I. P. Parkin, *Adv. Sci.* **2017**, *4*, 1600214; bT. Y. Ma, J. L. Cao, M. Jaroniec, S. Z. Qiao, *Angew. Chem. Int. Ed.* **2016**, *55*, 1138-1142; cT. Zhang, H. S. Zhou, *Angew. Chem. Int. Ed.* **2012**, *51*, 11062-11067; dL. Dai, Y. Xue, L. Qu, H. J. Choi, J. B. Baek, *Chem. Rev.* **2015**, *115*, 4823-4892; eR. R. Mitchell, B. M. Gallant, C. V. Thompson, Y. Shao-Horn, *Energy Environ. Sci.* **2011**, *4*, 2952-2958; fX. G. Wang, W. Li, D. H. Xiong, D. Y. Petrovykh, L. F. Liu, *Adv. Funct. Mater.* **2016**, *26*, 4067-4077; gZ. J. Liu, Z. H. Zhao, Y. Y. Wang, S. Dou, D. F. Yan, D. D. Liu, Z. H. Xia, S. Y. Wang, *Adv. Mater.* **2017**, *29*, 1606207; hZ. Y. Lu, W. W. Xu, J. Ma, Y. J. Li, X. M. Sun, L. Jiang, *Adv. Mater.* **2016**, *28*, 7155-7161; iN. Y. Cheng, Q. Liu, J. Q. Tian, Y. R. Xue, A. M. Asiri, H. F. Jiang, Y. Q. He, X. P. Sun, *Chem. Commun.* **2015**, *51*, 1616-1619; jM. S. Balogun, W. T. Qiu, H. Yang, W. J. Fan, Y. C. Huang, P. P. Fang, G. R. Li, H. B. Ji, Y. X. Tong, *Energy Environ. Sci.* **2016**, *9*, 3411-3416; kG. Li, X. L. Wang, M. H. Seo, S. Hemmati, A. P. Yu, Z. W. Chen, *J. Mater. Chem. A* **2017**, *5*, 10895-10901; lR. Chen, H. Y. Wang, J. W. Miao, H. B. Yang, B. Liu, *Nano Energy* **2015**, *11*, 333-340; mH. W. Huang, C. Yu, C. T. Zhao, X. T. Han, J. Yang, Z. B. Liu, S. F. Li, M. D. Zhang, J. S. Qiu, *Nano Energy* **2017**, *34*, 472-480.

[14] aB. G. Zhu, S. C. Tang, S. Vongehr, H. Xie, J. Zhu, X. K. Meng, *Chem. Commun.* **2016**, *52*, 2624-2627; bX. Wang, Y. Y. Wang, C. M. Zhao, Y. X. Zhao, B. Y. Yan, W. T. Zheng, *New J. Chem.* **2012**, *36*, 1902-1906.

[15] D. W. Wang, F. Li, J. P. Zhao, W. C. Ren, Z. G. Chen, J. Tan, Z. S. Wu, I. Gentle, G. Q. Lu, H. M. Cheng, *ACS Nano* **2009**, *3*, 1745-1752.

[16] aT. Y. Ma, J. R. Ran, S. Dai, M. Jaroniec, S. Z. Qiao, *Angew. Chem. Int. Ed.* **2015**, *54*, 4646-4650; bF. L. Meng, H. X. Zhong, D. Bao, J. M. Yan, X. B. Zhang, *J. Am. Chem. Soc.* **2016**, *138*, 10226-10231; cH.-F. Wang, C. Tang, B. Wang, B.-Q. Li, X. Cui, Q. Zhang, *Energy Storage Mater.* **2018**, *15*, 124-130.

[17] X. Y. Cai, B. Y. Xia, J. Franklin, B. S. Li, X. Wang, Z. Wang, L. W. Chen, J. Y. Lin, L. F. Lai, Z. X. Shen, *J. Mater. Chem. A* **2017**, *5*, 2488-2495.

[18] B. Bozzini, P. Bocchetta, A. Gianoncelli, C. Mele, M. Kiskinova, *Acta Chim. Slov.* **2014**, *61*, 263-271.

[19] C. Walter, K. Kummer, D. Vyalikh, V. Bruser, A. Quade, K. D. Weltmann, *J. Electrochem. Soc.* **2012**, *159*, F560-F569.

[20] Z. P. Chen, W. C. Ren, L. B. Gao, B. L. Liu, S. F. Pei, H. M. Cheng, *Nat. Mater.* **2011**, *10*, 424-428.

[21] X. Y. Cai, R. V. Hansen, L. L. Zhang, B. S. Li, C. K. Poh, S. H. Lim, L. W. Chen, J. L. Yang, L. F. Lai, J. Y. Lin, Z. X. Shen, *J. Mater. Chem. A* **2015**, *3*, 22043-22052.

[22] J. Fu, F. M. Hassan, J. D. Li, D. U. Lee, A. R. Ghannoum, G. Lui, M. A. Hoque, Z. W. Chen, *Adv. Mater.* **2016**, *28*, 6421-6428.

[23] X. Cai, B. Y. Xia, J. Franklin, B. Li, X. Wang, Z. Wang, L. Chen, J. Lin, L. Lai, Z. Shen, *J. Mater. Chem. A* **2017**, *5*, 2488-2495.

[24] aJ. L. Guan, Z. P. Zhang, J. Ji, M. L. Dou, F. Wang, *ACS Appl. Mater. Interfaces* **2017**, *9*, 30662-30669; bB. B. Huang, Y. C. Liu, Z. L. Xie, *J. Mater. Chem. A* **2017**, *5*, 23481-23488.

[25] M. Qiao, C. Tang, L. C. Tanase, C. M. Teodorescu, C. M. Chen, Q. Zhang, M. M. Titirici, *Mater. Horizons* **2017**, *4*, 895-899.

[26] aW. J. Niu, R. H. Zhu, H. Yan, H. B. Zeng, S. Cosnier, X. J. Zhang, D. Shan, *Carbon* **2016**, *109*, 402-410; bM. Qiao, C. Tang, G. He, K. Qiu, R. Binions, I. P. Parkin, Q. Zhang, Z. Guo, M. M. Titirici, *J. Mater. Chem. A* **2016**, *4*, 12658-12666; cJ. J. Wu, D. Zhang, Y. Wang, B. R. Hou, *J. Power Sources* **2013**, *227*, 185-190.

[27] aA. M. Abdelkader, N. Karim, C. Valles, S. Afroj, K. S. Novoselov, S. G. Yeates, *2D Mater.* **2017**, *4*, 035016; bQ. Q. Zhang, Y. Wang, B. Q. Zhang, K. R. Zhao, P. G. He, B. Y. Huang, *Carbon* **2018**, *127*, 449-458; cC. Z. Zhu, H. Li, S. F. Fu, D. Du, Y. H. Lin, *Chem. Soc. Rev.* **2016**, *45*, 517-531; dL. Ren, K. S. Hui, K. N. Hui, *J. Mater. Chem. A* **2013**, *1*, 5689-5694; eR. K. L. Tan, S. P. Reeves, N. Hashemi, D. G. Thomas, E. Kavak, R. Montazami, N. N. Hashemi, *J. Mater. Chem. A* **2017**, *5*, 17777-17803; fH. W. Liang, Z. Y. Wu, L. F. Chen, C. Li, S. H. Yu, *Nano Energy* **2015**, *11*, 366-376; gA. A. Mamedov, N. A. Kotov, M. Prato, D. M. Guldi, J. P. Wicksted, A. Hirsch, *Nat. Mater.* **2002**, *1*, 190-194; hV. L. Pushparaj, M. M. Shaijumon, A. Kumar, S. Murugesan, L. Ci, R. Vajtai, R. J. Linhardt, O. Nalamasu, P. M. Ajayan, *Proc. Natl. Acad. Sci. U. S. A.* **2007**, *104*, 13574-13577; iL. L. Liu, J. Wang, Y. Y. Hou, J. Chen, H. K. Liu, J. Z. Wang, Y. P. Wu, *Small* **2016**, *12*, 602-611.

[28] aS. Chen, J. J. Duan, M. Jaroniec, S. Z. Qiao, *Adv. Mater.* **2014**, *26*, 2925-2930; bN. Díez, C. Botas, R. Mysyk, E. Goikolea, T. Rojo, D. Carriazo, *J. Mater. Chem. A* **2018**, *6*, 3667-3673; cW. C. Li, A. H. Lu, F. Schuth, *Chem. Mater.* **2005**, *17*, 3620-3626.

[29] aN. Mansor, T. S. Miller, I. Dedigama, A. B. Jorge, J. J. Jia, V. Brazdova, C. Mattevi, C. Gibbs, D. Hodgson, P. R. Shearing, C. A. Howard, F. Cora, M. Shaffer, D. J. L. Brett, P. F. McMillan, *Electrochim. Acta* **2016**, *222*, 44-57; bS. Chen, J. Duan, J. Ran, M. Jaroniec, S. Z. Qiao, *Energy Environ. Sci.* **2013**, *6*, 3693-3699.

[30] Y. W. Cheng, H. B. Zhang, C. V. Varanasi, J. Liu, *Sci. Rep.* **2013**, *3*, 3195.

[31] Y. Zhang, J. J. Magan, W. J. Blau, *Sci. Rep.* **2014**, *4*, 4822.

[32] D. Li, M. B. Müller, S. Gilje, R. B. Kaner, G. G. Wallace, *Nat. Nanotechnol.* **2008**, *3*, 101.

[33] aK. Wang, T. Feng, M. Qian, H. I. Ding, Y. W. Chen, Z. O. Sun, *Appl. Surf. Sci.* **2011**, *257*, 5808-5812; bJ. Y. Chen, Y. L. Guo, L. P. Huang, Y. Z. Xue, D. C. Geng, H. T. Liu, B. Wu, G. Yu, W. P. Hu, Y. Q. Liu, D. B. Zhu, *Philos. Trans. Royal Soc. A* **2014**, *372*, 20130017.

[34] G. Eda, G. Fanchini, M. Chhowalla, *Nat. Nanotechnol.* **2008**, *3*, 270-274.

[35] D. X. Ji, S. J. Peng, J. Lu, L. L. Li, S. Y. Yang, G. R. Yang, X. H. Qin, M. Srinivasan, S. Ramakrishna, *J. Mater. Chem. A* **2017**, *5*, 7507-7515.

[36] aN. Wu, Y. D. Wang, Y. P. Lei, B. Wang, C. Han, Y. Z. Gou, Q. Shi, D. Fang, *Sci. Rep.* **2015**, *5*, 17396; bY. Li, S. M. Chen, D. W. Xi, Y. N. Bo, R. Long, C. M. Wang, L. Song, Y. J. Xiong, *Small* **2018**, *14*, 1702109; cY. F. Zhao, J. Q. Zhang, X. Guo, H. B. Fan, W. J. Wu, H. Liu, G. X. Wang, *J. Mater. Chem. A* **2017**, *5*, 19672-19679.

[37] Y. Li, L. L. Zou, J. Li, K. Guo, X. W. Dong, X. W. Li, X. Z. Xue, H. F. Zhang, H. Yang, *Electrochim. Acta* **2014**, *129*, 14-20.

[38] aZ. Liu, H. G. Nie, Z. Yang, J. Zhang, Z. P. Jin, Y. Q. Lu, Z. B. Xiao, S. M. Huang, *Nanoscale* **2013**, *5*, 3283-3288; bY. Xie, D. Kocaefe, C. Chen, Y. Kocaefe, *J. Nanomater.* **2016**, *2016*, 2302595.

[39] C. W. Foster, M. P. Down, Y. Zhang, X. B. Ji, S. J. Rowley-Neale, G. C. Smith, P. J. Kelly, C. E. Banks, *Sci. Rep.* **2017**, *7*, 42233.

[40] S. D. Lacey, D. J. Kirsch, Y. Li, J. T. Morgenstern, B. C. Zarket, Y. Yao, J. Dai, L. Q. Garcia, B. Liu, T. Gao, S. Xu, S. R. Raghavan, J. W. Connell, Y. Lin, L. Hu, *Adv. Mater.* **2018**, *30*, 1705651.

[41] H. Wei, K. Li, W. G. Liu, H. Meng, P. X. Zhang, C. Y. Yan, *Adv. Eng. Mater.* **2017**, *19*, 1700341.

[42] D. A. Dikin, S. Stankovich, E. J. Zimney, R. D. Piner, G. H. B. Dommett, G. Evmenenko, S. T. Nguyen, R. S. Ruoff, *Nature* **2007**, *448*, 457-460.

[43] F. Song, W. Li, G. Han, Y. Sun, *ACS Applied Energy Materials* **2018**, *1*, 3-8.

[44] aC. B. Ouyang, S. Feng, J. Huo, S. Wang, *Green Energy Environ.* **2017**, *2*, 134-141; bY. X. Li, D. F. Yan, Y. Q. Zou, C. Xie, Y. Y. Wang, Y. Q. Zhang, S. Y. Wang, *J. Mater. Chem. A* **2017**, *5*, 25494-25500.

[45] aA. J. Esswein, M. J. McMurdo, P. N. Ross, A. T. Bell, T. D. Tilley, *The Journal Of Physical Chemistry C* **2009**, *113*, 15068-15072; bG. Liu, D. Y. He, R. Yao, Y. Zhao,

J. P. Li, *Nano Res.* **2018**, *11*, 1664-1675; cF. L. Li, Q. Shao, X. Q. Huang, J. P. Lang, *Angew. Chem. Int. Ed.* **2018**, *57*, 1888-1892.

[46] D. K. Huang, S. Li, X. H. Zhang, Y. Z. Luo, J. Xiao, H. Chen, *Carbon* **2018**, *129*, 468-475.

[47] Y. Yi, J. Tornow, E. Willinger, M. G. Willinger, C. Ranjan, R. Schlogl, *ChemElectroChem* **2015**, *2*, 1929-1937.

[48] M. Sevilla, A. B. Fuertes, *Carbon* **2006**, *44*, 468-474.

[49] aX. Ren, X. Q. Ji, Y. C. Wei, D. Wu, Y. Zhang, M. Ma, Z. Liu, A. M. Asiri, Q. Wei, X. P. Sun, *Chem. Commun.* **2018**, *54*, 1425-1428; bY. Z. Xu, C. Z. Yuan, X. P. Chen, *J. Solid State Chem.* **2017**, *256*, 124-129; cX. D. Wang, Y. Cao, Y. Teng, H. Y. Chen, Y. F. Xu, D. B. Kuang, *ACS Appl. Mater. Interfaces* **2017**, *9*, 32812-32819.

[50] B. A. Lu, D. X. Cao, P. Wang, G. L. Wang, Y. Y. Gao, *Int. J. Hydrogen Energy* **2011**, *36*, 72-78.

[51] N. T. Suen, S. F. Hung, Q. Quan, N. Zhang, Y. J. Xu, H. M. Chen, *Chem. Soc. Rev.* **2017**, *46*, 337-365.

[52] aY. C. Wei, X. Ren, H. M. Ma, X. Sun, Y. Zhang, X. Kuang, T. Yan, H. X. Ju, D. Wu, Q. Wei, *Chem. Commun.* **2018**, *54*, 1533-1536; bJ. Q. Chi, K. L. Yan, Z. Xiao, B. Dong, X. Shang, W. K. Gao, X. Li, Y. M. Chai, C. G. Liu, *Int. J. Hydrogen Energy* **2017**, *42*, 20599-20607; cZ. G. Ye, T. Li, G. Ma, Y. H. Dong, X. L. Zhou, *Adv. Funct. Mater.* **2017**, *27*, 1704083.

[53] H. J. Yin, L. X. Jiang, P. R. Liu, M. Al-Mamun, Y. Wang, Y. L. Zhong, H. G. Yang, D. Wang, Z. Y. Tang, H. J. Zhao, *Nano Res.* **2017**, *doi: 10.1007/s12274-017-1886-7*.

[54] aJ. Duan, S. Chen, A. Vasileff, S. Z. Qiao, *ACS Nano* **2016**, *10*, 8738-8745; bW. J. Zhou, X. J. Wu, X. H. Cao, X. Huang, C. L. Tan, J. Tian, H. Liu, J. Y. Wang, H. Zhang, *Energy Environ. Sci.* **2013**, *6*, 2921–2924; cH. N. Ren, Z. H. Huang, Z. Y. Yang, S. J. Tang, F. Y. Kang, R. T. Lv, *J. Energy Chem.* **2017**, *26*, 1217-1222; dJ. T. Ren, Z. P. Hu, C. Chen, Y. P. Liu, Z. Y. Yuan, *J. Energy Chem.* **2017**, *26*, 1196-1202.

[55] Z. Lu, W. Xu, W. Zhu, Q. Yang, X. Lei, J. Liu, Y. Li, X. Sun, X. Duan, *Chem. Commun.* **2014**, *50*, 6479-6482.

[56] H. Q. Zhou, F. Yu, J. Y. Sun, R. He, S. Chen, C. W. Chu, Z. F. Ren, *Proc. Natl. Acad. Sci. U. S. A.* **2017**, *114*, 5607-5611.

[57] aJ. X. Feng, S. H. Ye, H. Xu, Y. X. Tong, G. R. Li, *Adv. Mater.* **2016**, *28*, 4698-4703; bJ. X. Feng, H. Xu, Y. T. Dong, S. H. Ye, Y. X. Tong, G. R. Li, *Angew. Chem. Int. Ed.* **2016**, *55*, 3694-3698.

[58] aJ. Y. C. Chen, L. N. Dang, H. F. Liang, W. L. Bi, J. B. Gerken, S. Jin, E. E. Alp, S. S. Stahl, *J. Am. Chem. Soc.* **2015**, *137*, 15090-15093; bL. Trotochaud, S. L. Young, J. K. Ranney, S. W. Boettcher, *J. Am. Chem. Soc.* **2014**, *136*, 6744-6753; cH. Zhang, Y. Zhou, C. G. Li, S. L. Chen, L. Liu, S. W. Liu, H. M. Yao, H. Q. Hou, *Carbon* **2015**, *95*, 388-395.

[59] Z. H. Xiao, Y. Wang, Y. C. Huang, Z. X. Wei, C. L. Dong, J. M. Ma, S. H. Shen, Y. F. Li, S. Y. Wang, *Energy Environ. Sci.* **2017**, *10*, 2563-2569.

[60] Q. Zhang, H. X. Zhong, F. L. Meng, D. Bao, X. B. Zhang, X. L. Wei, *Nano Res.* **2018**, *11*, 1294-1300.
[61] C. Z. Yuan, S. L. Zhong, Y. F. Jiang, Z. K. Yang, Z. W. Zhao, S. J. Zhao, N. Jiang, A. W. Xu, *J. Mater. Chem. A* **2017**, *5*, 10561-10566.
[62] C. Z. Yuan, Z. T. Sun, Y. F. Jiang, Z. K. Yang, N. Jiang, Z. W. Zhao, U. Y. Qazi, W. H. Zhang, A. W. Xu, *Small* **2017**, *13*, 1604161.
[63] aP. Chen, K. Xu, Z. Fang, Y. Tong, J. Wu, X. Lu, X. Peng, H. Ding, C. Wu, Y. Xie, *Angew. Chem. Int. Ed.* **2015**, *54*, 14710-14714; bX. Q. Ji, L. Cui, D. N. Liu, S. Hao, J. Q. Liu, F. L. Qu, Y. J. Ma, G. Du, A. M. Asiri, X. P. Sun, *Chem. Commun.* **2017**, *53*, 3070-3073.
[64] aC. C. Huang, C. Li, G. Q. Shi, *Energy Environ. Sci.* **2012**, *5*, 8848-8868; bX. W. Yu, M. Zhang, W. J. Yuan, G. Q. Shi, *J. Mater. Chem. A* **2015**, *3*, 6921-6928; cF. Song, X. L. Hu, *Nat. Commun.* **2014**, *5*, 4477.
[65] F. Banhart, J. Kotakoski, A. V. Krasheninnikov, *ACS Nano* **2011**, *5*, 26-41.
[66] aX. Y. Lu, W. L. Yim, B. H. R. Suryanto, C. Zhao, *J. Am. Chem. Soc.* **2015**, *137*, 2901-2907; bC. Tang, H. F. Wang, X. Chen, B. Q. Li, T. Z. Hou, B. S. Zhang, Q. Zhang, M. M. Titirici, F. Wei, *Adv. Mater.* **2016**, *28*, 6845-6851.
[67] S. Chen, S. Z. Qiao, *ACS Nano* **2013**, *7*, 10190–10196
[68] S. Chen, J. J. Duan, J. R. Ran, S. Z. Qiao, *Adv. Sci.* **2015**, *2*, 1400015.
[69] X. W. Yu, M. Zhang, J. Chen, Y. R. Li, G. Q. Shi, *Adv. Energy Mater.* **2016**, *6*, 1501492.
[70] Y. P. Zhu, J. Ran, S. Z. Qiao, *ACS Appl. Mater. Interfaces* **2017**, *9*, 41980-41987.
[71] X. Y. Sun, R. Wang, D. S. Su, *Chinese J. Catal.* **2013**, *34*, 508-523.
[72] aM. H. Shao, Q. W. Chang, J. P. Dodelet, R. Chenitz, *Chem. Rev.* **2016**, *116*, 3594-3657; bS. Sui, X. Y. Wang, X. T. Zhou, Y. H. Su, S. Riffatc, C. J. Liu, *J. Mater. Chem. A* **2017**, *5*, 1808-1825.
[73] aS. F. Fu, C. Z. Zhu, J. H. Song, D. Du, Y. H. Lin, *Adv. Energy Mater.* **2017**, *7*, 1700363; bZ. H. Xia, L. An, P. K. Chen, D. G. Xia, *Adv. Energy Mater.* **2016**, *6*, 1600458; cY. L. Zhu, W. Zhou, Z. P. Shao, *Small* **2017**, *13*, 1603793.
[74] S. Mentus, *J. Electroanal. Chem.* **2015**, *738*, 47-50.
[75] D. Liu, X. P. Zhang, Z. C. Sun, T. Y. You, *Nanoscale* **2013**, *5*, 9528-9531.
[76] Y. X. Li, X. B. Ge, L. D. Y. Wang, J. Liu, Y. Wang, L. X. Feng, *RSC Adv.* **2017**, *7*, 11568-11571.
[77] U. Pasaogullari, C. Y. Wang, *Electrochim. Acta* **2004**, *49*, 4359-4369.
[78] Y. Q. Wang, L. Tao, Z. H. Xiao, R. Chen, Z. Q. Jiang, S. Y. Wang, *Adv. Funct. Mater.* **2018**, *28*, 1705356.
[79] M. Qiao, C. Tang, L. C. Tanase, C. M. Teodorescu, C. Chen, Q. Zhang, M.-M. Titirici, *Mater. Horizons* **2017**, *4*, 895-899.
[80] J. Suntivich, H. A. Gasteiger, N. Yabuuchi, H. Nakanishi, J. B. Goodenough, Y. Shao-Horn, *Nat. Chem.* **2011**, *3*, 546-550.
[81] aK. L. Pickrahn, S. W. Park, Y. Gorlin, H. B. R. Lee, T. F. Jaramillo, S. F. Bent, *Adv. Energy Mater.* **2012**, *2*, 1269-1277; bC. Tang, B. Wang, H. F. Wang, Q. Zhang, *Adv. Mater.* **2017**, *29*, 1703185; cH. F. Wang, C. Tang, B. Wang, B. Q. Li, Q.

Zhang, *Adv. Mater.* **2017**, *29*, 1702327; dS. Dou, L. Tao, J. Huo, S. Y. Wang, L. M. Dai, *Energy Environ. Sci.* **2016**, *9*, 1320-1326; eH. F. Wang, C. Tang, X. L. Zhu, Q. Zhang, *J. Mater. Chem. A* **2016**, *4*, 3379-3385; fY. Gorlin, T. F. Jaramillo, *J. Am. Chem. Soc.* **2010**, *132*, 13612-13614; gF. Y. Cheng, J. A. Shen, B. Peng, Y. D. Pan, Z. L. Tao, J. Chen, *Nat. Chem.* **2011**, *3*, 79-84.

[82] G. L. Chai, K. P. Qiu, M. Qiao, M. M. Titirici, C. X. Shang, Z. X. Guo, *Energy Environ. Sci.* **2017**, *10*, 1186-1195.

[83] W. T. Hong, M. Risch, K. A. Stoerzinger, A. Grimaud, J. Suntivich, Y. Shao-Horn, *Energy Environ. Sci.* **2015**, *8*, 1404-1427.

[84] Y. Zhan, M. H. Lu, S. L. Yang, C. H. Xu, Z. L. Liu, J. Y. Lee, *ChemCatChem* **2016**, *8*, 372-379.

[85] S. Dou, X. Y. Li, L. Tao, J. Huo, S. Y. Wang, *Chem. Commun.* **2016**, *52*, 9727-9730.

[86] S. S. Shinde, C. H. Lee, A. Sami, D. H. Kim, S. U. Lee, J. H. Lee, *ACS Nano* **2017**, *11*, 347-357.

[87] G. Liu, P. Niu, C. H. Sun, S. C. Smith, Z. G. Chen, G. Q. Lu, H. M. Cheng, *J. Am. Chem. Soc.* **2010**, *132*, 11642-11648.

[88] Q. Liu, Y. Wang, L. Dai, J. Yao, *Adv. Mater.* **2016**, *28*, 3000-3006.

[89] aW. Liu, M. S. Song, B. Kong, Y. Cui, *Adv. Mater.* **2017**, *29*, 1603436; bL. Wen, F. Li, H. M. Cheng, *Adv. Mater.* **2016**, *28*, 4306-4337.

[90] J. C. Li, P. X. Hou, S. Y. Zhao, C. Liu, D. M. Tang, M. Cheng, F. Zhang, H. M. Cheng, *Energy Environ. Sci.* **2016**, *9*, 3079-3084.

Table of content

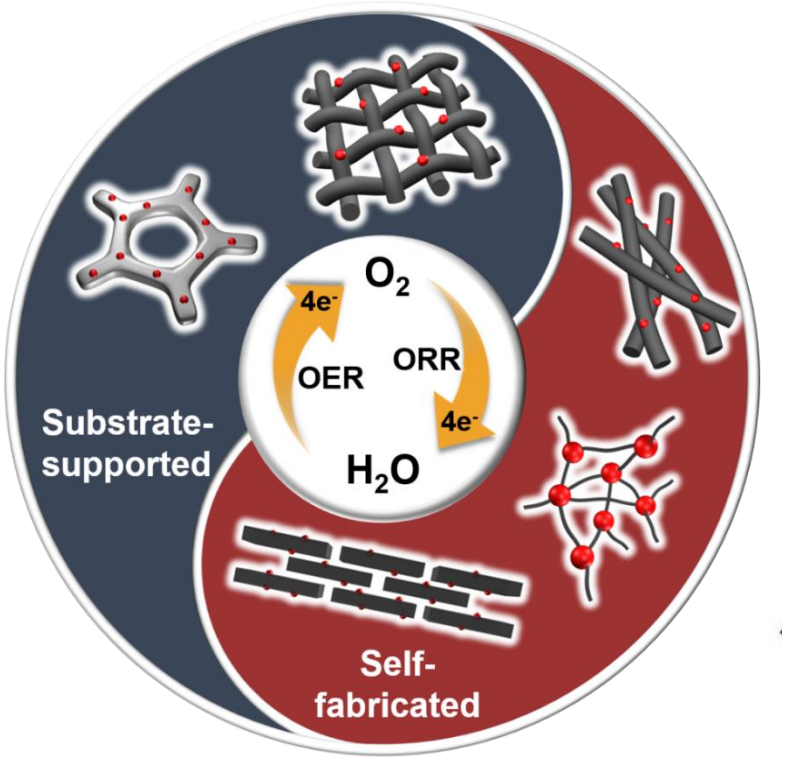

This review summarizes fabrication techniques used in synthesis of non-noble metal electrocatalysts for ORR and OER in a freestanding form, their performance, characterisation and substrate materials used in the process. Applications of reviewed electrocatalysts are also discussed highlighting current performance and stability of zinc-air batteries based on the freestanding electrodes.